FLOW MODULATION AND FORCE CONTROL OF FLAPPING WINGS

XINYAN DENG
PURDUE UNIVERSITY

10/29/2014
Final Report

Flow Modulation and Force Control of Flapping Wings

Grant number: AFOSR FA9550-11-1-0058

Principal Investigator (PI): Xinyan Deng, Purdue University

Co-PI: Haibo Dong, University of Virginia

Contents

List of Figures

Project name: Flow Modulation and Force Control of Flapping Wings
Grant number: AFOSR FA9550-11-1-0058
Principal Investigator (PI): Xinyan Deng, Purdue University
        Co-PI: Haibo Dong, University of Virginia

---

1. Proposed research and technical objectives

Flapping-wing offers unique force enhancement mechanisms over conventional flight methods for design of micro air vehicles (MAVs), especially in the low Reynolds number (Re) regime. The inherently unsteady nature of flapping kinematics is responsible for the primary force production [1], and also differentiates flapping-wing motion from conventional fixed and rotary wing configurations. From previous observation, the unsteady aerodynamic phenomena of flapping mechanism are not only sensitive to variations in the wing kinematics but also for the wing morphing [2,3]. Results have shown that the dynamically changed wing surface, either actively or passively deformed, would potentially provide new aerodynamic mechanisms of force productions over completely rigid wings in flying [4]. From morphing wing study in fixed or rotary wing aircrafts, the moving surface flow control concept can be achieved in three ways: 1) articulated flaps and/or slats [5]; 2) surface flow control devices [6]; and 3) continuously deforming surfaces [7]. Among them, the dynamic flow control concept via trailing-edge flap (TEF) is presumed to be more applicable serving for novel MAVs wing designs, in terms of reduced size of control surface, complexity of moving surface control, weight of MAVs and so on. However, there is a lack of study of the effects of TEF on a flapping wing in computations and experiments, especially when the flap is in dynamic motion with respect to the leading-edge motion. In this funded work, we built up a team with experts from two institutes and hope to address the following basic questions about the aerodynamics of flapping flight:

1. What are the aerodynamic effects of dynamic trailing-edge flap motion when it moves through the flow?

2. What is the mutual interaction between fluid flow patterns and wing morphology patterns?

3. What is the proper way(s) to characterize wing flexibility from aerodynamics point of view?

4. What is the overall far field flow structure of flapping wings?

2. Experimental study

In this part, three sections regarding the experimental study on the proposed topic are presented. We briefly summarize these works in the following.

(1) Aerodynamics of static and dynamic trailing edge deflection in flapping wings.
   - ➢ Experiments on passively flexible and cambered wing during flapping motion at fixed trailing edge angles were conducted. Force measurements and PIV results revealed that wing flexing/camber correlates closely with the size of the leading edge vortex and the magnitude of the aerodynamic forces.
   - ➢ To find out the dynamic response due to the fluttering trailing edges, we measured the forces while keeping the trailing edge flexing/camber motion sinusoidal with different phase delay from the leading edge motion. We found that both phase delay and fluttering frequency have great effects on lift force magnitudes.

(2) Aerodynamics of dynamic trailing edge deflection in translating wings.
   - ➢ We conducted a systematic experimental study to investigate the aerodynamic effects of active trailing edge flap deflection on a high aspect ratio wing translating from rest at a high angle of attack (AoA). We varied the timing and speed of the trailing-edge flap deflection which acted to enhance the camber, and measured the resulting aerodynamic effects using a combination of direct force measurements and two-dimensional (2D) flow measurements. The results indicated that the force and flow characteristics depend strongly on the timing of deflection, but relatively weakly on speed.

(3) Understanding the flow physics of flapping/revolving wings
   - ➢ We investigated the complex and interconnected vortical structures and dynamics generated by revolving wings. The three-dimensional velocity and vorticity fields were represented with respect to the base axes of rotating Cartesian reference frames, and the second invariant of the velocity gradient was evaluated and used as a criterion to identify two core vortex structures. Using the fundamental vorticity equation, we evaluated the convection, stretching and tilting of vorticity in the rotating wing frame to understand the generation and evolution of vorticity. Based on these data, we propose that the vorticity generated at the leading edge is carried away by strong tangential flow into the wake and travels downwards with the induced downwash.
   - ➢ We investigated the three-dimensional vortex wake structure in both the near and far field of a dynamically-scaled flapping wing, using volumetric three-component velocimetry. A single wing, with shape and kinematics similar to those of a fruit fly, was examined. We found that the overall result of the wing action is to create an integrated vortex structure consisting of a tip vortex (TV), trailing-edge shear layer (TESL) and leading-edge vortex (LEV). The TESL rolls up into a root vortex (RV) as it is shed from the wing, and together with the TV, contracts radially and stretches tangentially in the downstream wake.To understand the spatial and temporal distribution of the complex three

dimensional vortex wake structure, we quantified the wake structure and its evolution throughout a wing stroke. We found that general vortex wake structure maintains a quite consistent form: vortex rings in the near-field and two shear layers in the far-field. In specific, vortex rings shed periodically from the wings and are linked to each other in successive strokes. In the far-field, the shed vortex rings evolve into two parallel shear layers with dominant vorticity convected from tip and root vortices. The shear layers are nearly stationary in space compared to the periodic vortex rings shed in the near field. In addition, downwash passes through the centers of the vortex rings and extends downward between the two shear layers.

➤ In hovering insects and hummingbirds, flapping wings create significant downwash in the wake. Therefore by placing the smoke wire close to the leading edge of the wing, we expect the downwash to drag the smoke particles into the wake and to form smoke patterns that visualize the flow structure generated by the flapping wings. To exam this idea, we tested a pair of Cicada wings driven by a robotic insect model using four-bar mechanism. The robotic insect model achieves a flapping amplitude of 130° with the angle of attack limited to 45°. The smoke was generated using paraffin oil heated along a 0.25 mm in diameter stainless steel wire. A high speed camera was used to record the smoke pattern at 1000 frame/s.

2.1 Aerodynamics of static/dynamic trailing edge deflection in flapping wings

1) Experiments on static trailing edge deflection during flapping motion

To examine how static camber affect the wing force generation, we performed the experiments in an oil tank with dynamically scaled robotic wings. The wing accelerate quickly to reach a constant angular velocity and remains until the end of the stroke, then decelerate and turn back. The wing flapping frequency is 0.25 Hz , and stroke angle is 180 degree. We used the fixed angle of attack for the wing (38and 52 degree) and for the statically cambered trailing edge as well(-20~20 degree, negative means flexion and positive value represent camber). The constant angular velocity generated the lift force plateau. We plot the mean lift value in-between the translational phase(Figure 1).
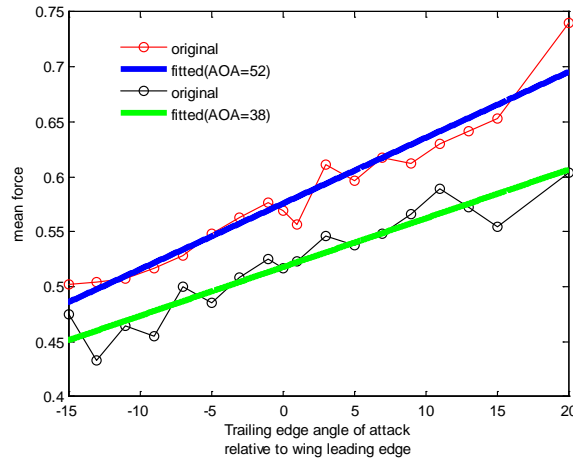
Figure 1. Lift force on the wing model with static camber and flexion

As we can find in the figure, there are very good linearity between the trailing edge angle and the aerodynamic lift force generation. As the trailing edge rotate toward the downstream(flexion), the force generated is smaller than the un-rotated case. To find out the flow pattern and strength change when the trailing edge angle change, we performed PIV measurements on the selected TE angles(-20, 0 and 20 degree). Fig 2 shows the leading edge vortex change as the TE angle changes. The flexion (negative camber) wing has a weaker LEV while the flat one has a stronger LEV. As the positive camber appears, we cannot see the obvious increase in strength of the LEV. However, the size of the LEV did change slightly.

The LEV is commonly recognized to be able to generate a low pressure center so that the lift force will be increased as the LEV appear. Here, we found that the TE camber correlates with the LEV strength and may be the cause for lift force change.
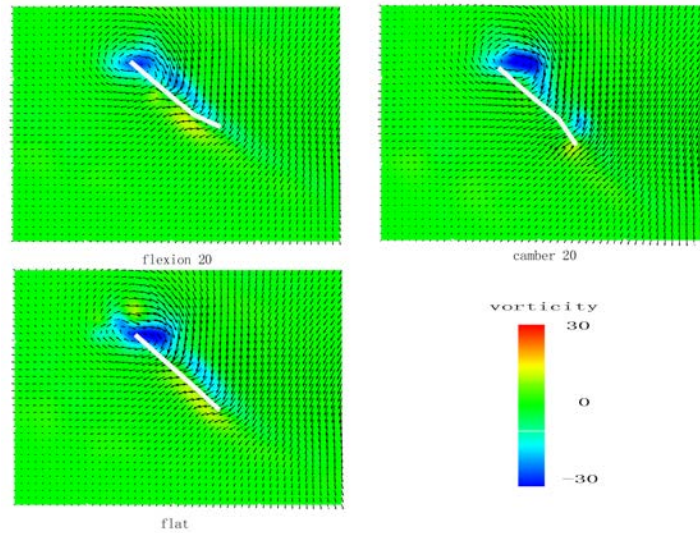
Figure 2. The PIV results of the flexion, camber and fat wings.

2) Experiments on dynamically fluttering trailing edge during flapping motion

Active camber was tested on a flapping wing model in the oil tank. Robotic flapper equipped with DC motors drove the wing model, and the imbedded servo motor could flap the model trailing edge(TE) at frequency from 0-7 Hz. To find out the dynamic force response due to the fluttering TE, we tested the forces while keeping flapping frequency at 0.25 Hz and TE sinusoidal at 0-7 Hz with phase delay from 0-2Pi. As we can see from Figure 3, as the delay changed, the mean lift force generation is different in magnitudes. As the delay increase from zero to π the lift force increase and reached to the peak value, then it started to decrease as the delay go higher. We also examined the flutter frequency effects by testing cases with TE fluttering frequency from 0 Hz to 7 Hz. Obviously, at the 0.25 Hz TE frequency, the force peaks. The camber was guaranteed at such frequency and phase delay, so that the force was high than other cases, where partial or entire stroke not camber but flexion did appear. Therefore, both phase delay and fluttering frequency have great effects on lift force magnitudes.
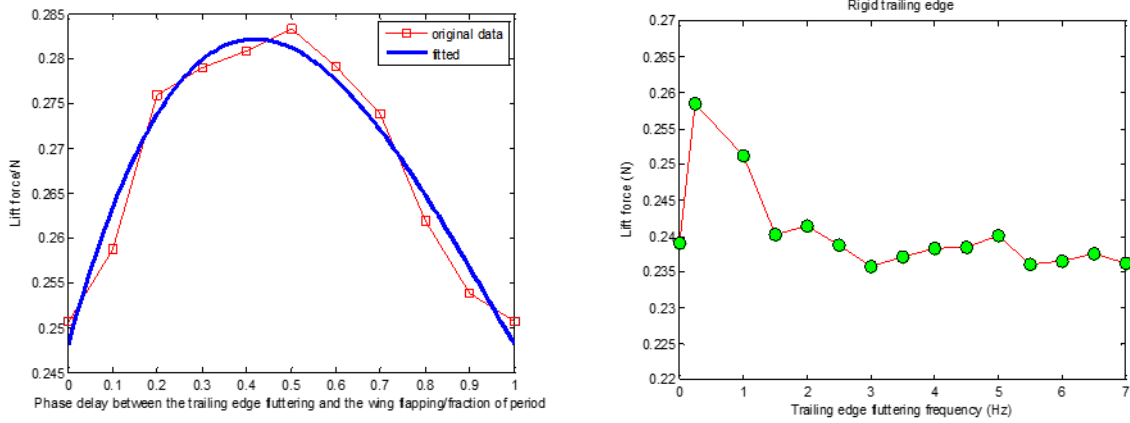
Figure 3. Left: Lift force as the function of the trailing edge delay; **Right:** Lift force as a function of the trailing edge flapping frequency.

Concluding Remarks:

Cambered wings can generate more lifts with wing span unchanged. This can benefit the wing flight animals or MAVs at time in need of short period of high lifts. Some previous research on flexible wing showed us great correlation between the wing flexibility and the aerodynamic force generation. Here, we can find an almost perfect consistency of aerodynamic force from flexion to camber. At static case, they are even in linearity, which provides a practical guidance to the MAV designers on the wing design.

We studied the flapping amplitude of the trailing edge, frequency of the trailing edge and the phase delay between the leading and trailing edge flapping motion. The amplitude has similar effects on aerodynamics except that the linearity changed to 3rd order polynomial. The Phase delay is so important that it can change the sign of lift increment because in the dynamics motion, camber and flexion has to be re-defined according to the leading edge flapping direction, which means the camber can also be flexion if the coming velocity direction changed. Thus, the timing is crucial. The frequency also can change the force generation, considering that at the same frequency of leading edge and keep the phase delay optimized for lift, the wing can generated more than 10% lift than at other frequency. In fact, the frequency and phase delay are working together and the longer the cambered portion, the higher the lift force [38].

2.2 Aerodynamics of dynamic trailing edge deflection in translating wings

We conducted a comprehensive experimental study to investigate the aerodynamic effects of active trailing edge flap deflection on a high aspect ratio wing translating from rest at a high angle of attack (AoA). We varied the timing and speed of the trailing-edge flap deflection which acted to enhance the camber, and measured the resulting aerodynamic effects using a combination of direct force measurements and two-dimensional (2D) flow measurements. The results indicated that the force and flow characteristics depend strongly on the timing of deflection, but relatively weakly on speed. This is because the force and vortical flow structure are more sensitive to the timing of flap deflection relative to the shedding of starting vortex and

11

leading edge vortex. When the trailing-edge flap deflection occurred slightly before the starting vortex (SV) was shed, the lift performance was greatly improved with the instantaneous lift peak doubling and averaged lift increasing by 20% compared to the case in a wing in which the trailing-edge flap deflected before wing translation (Figure 4). However, when the flap deflected during or slightly after the leading edge vortex (LEV) shedding, the lift was significantly reduced by the disturbed development of leading edge vortex. The force measurement results also imply that the trailing-edge flap deflection occurs before wing translation do not augment lift but increase drag, thus ensuring that the lift-drag ratio is lower as compared to the case of noncambered wing.
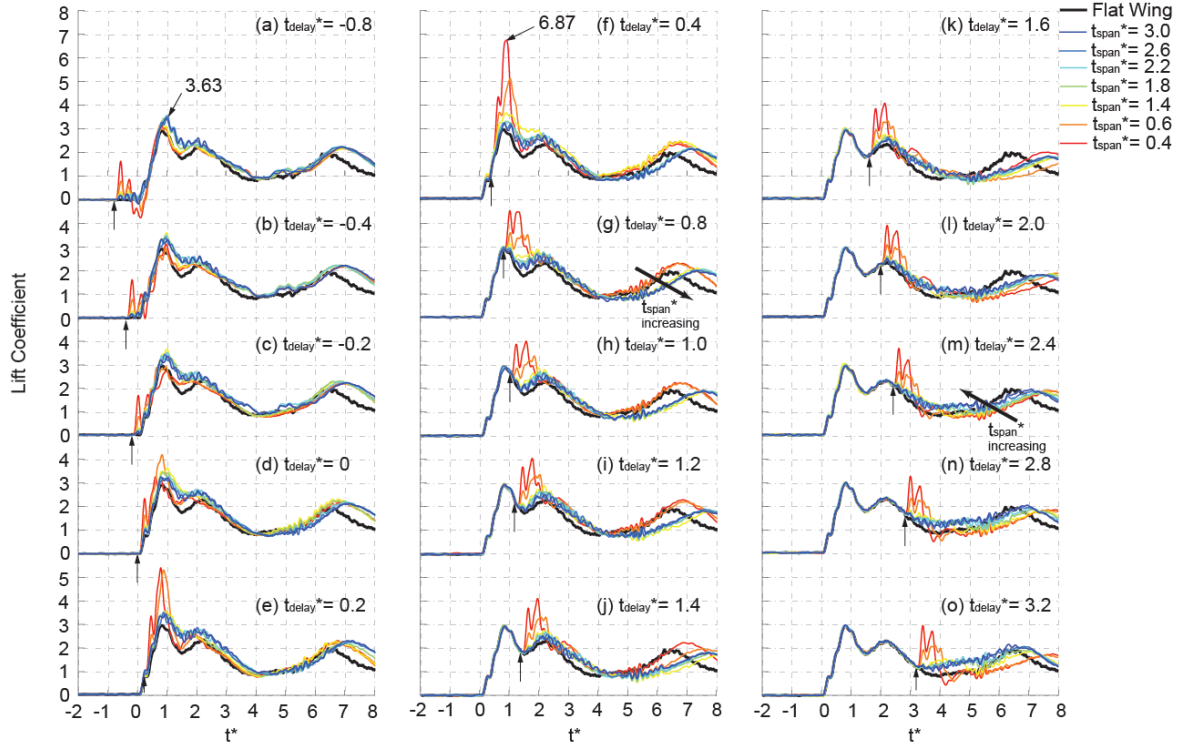
Figure 4. Instantaneous lift coefficient versus normalized time; Lift coefficient curves under the same deflection timing are plotted together in the same group (a-o). Black arrows indicate the instant when the wing starts to deflect. Black curves are the lift coefficient on the non-deflected flat wing while the other color coded curves present the lift coefficient on the wing with different deflection speeds

Therefore, by proper designing the flap kinematics relative to the vortex shedding events, significant improvement on force performance can be achieved. In particular, when the wing deflects slightly before the SV shedding with relatively fast speed, the wing produces maximum lift. However, if the wing deflects during or slightly after the LEV shedding, the lift is substantially reduced and close to that of the uncambered wing. It is also shown that by deflecting the flap within a certain range of timing at moderate speed, the vortex shedding on the wing changes dramatically and leads to four different patterns which can be directly related to four regions in the average lift contour plots. First, when the wing deflects before SV shedding, SV is enhanced by the deflection and a large lift peak is observed (Figure 5). Second, when the

wing deflects between shedding of SV and LEV, a second TEV is shed in addition to the SV and a moderate average lift is observed (Figure 6).
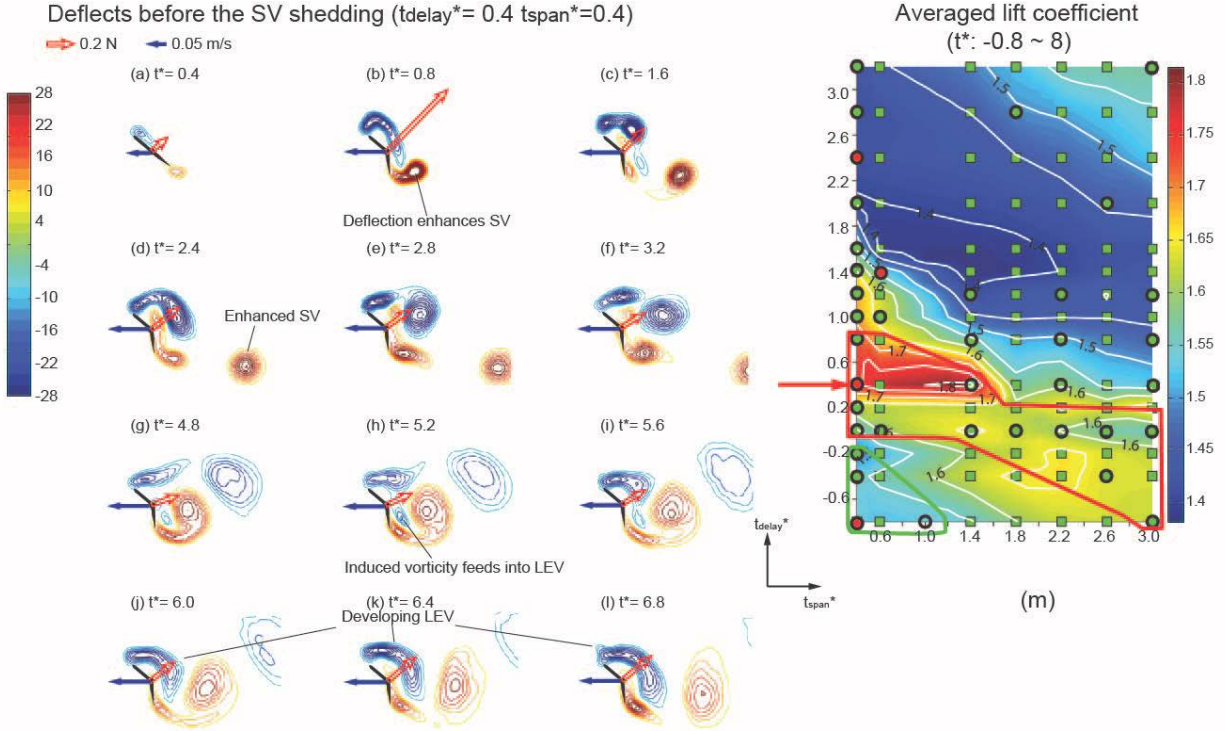
Figure 5. A typical flow in region II at tdelay*=0.4 and tspan*=0.4 (b) SV was enhanced by flap deflection and the net force had a significant increase. (h) Induced negative vorticity was feed into the LEV. (m) Region II with high average lift, highlighted by red loop.

Third, when the flap deflects during or slightly after LEV shedding, it affects the shedding of LEV and delays the development of circulation, resulting in a low average lift due to the reduced LEV strength (Figure 7). Fourth, when the wing deflects before the onset of translation at a rapid rate, a low average lift is observed as the force and flow structures are similar to those of the pre-cambered wing. Therefore, there is an unequivocal strong correlation between the SV strength and lift production (Figure 8).

Comparing to the active cambering on the 2D translating wing where only the leading edge and tailing edge vortex present, the active morphing on the flapping wing is surely a different and complicated story. Especially considering quantitative and thorough description of wake topology was not available, it is very necessary to first have a thorough understanding on the wake topology of hovering wing before studying the active camber on the flapping wing. In order to have a basic reference and knowledge about the highly unsteady and 3 dimensional flow on flapping wing, in the frame of this project, volumetric flow measurements were performed on two types of wing motions by using the V3V volumetric flow measurement system.

13
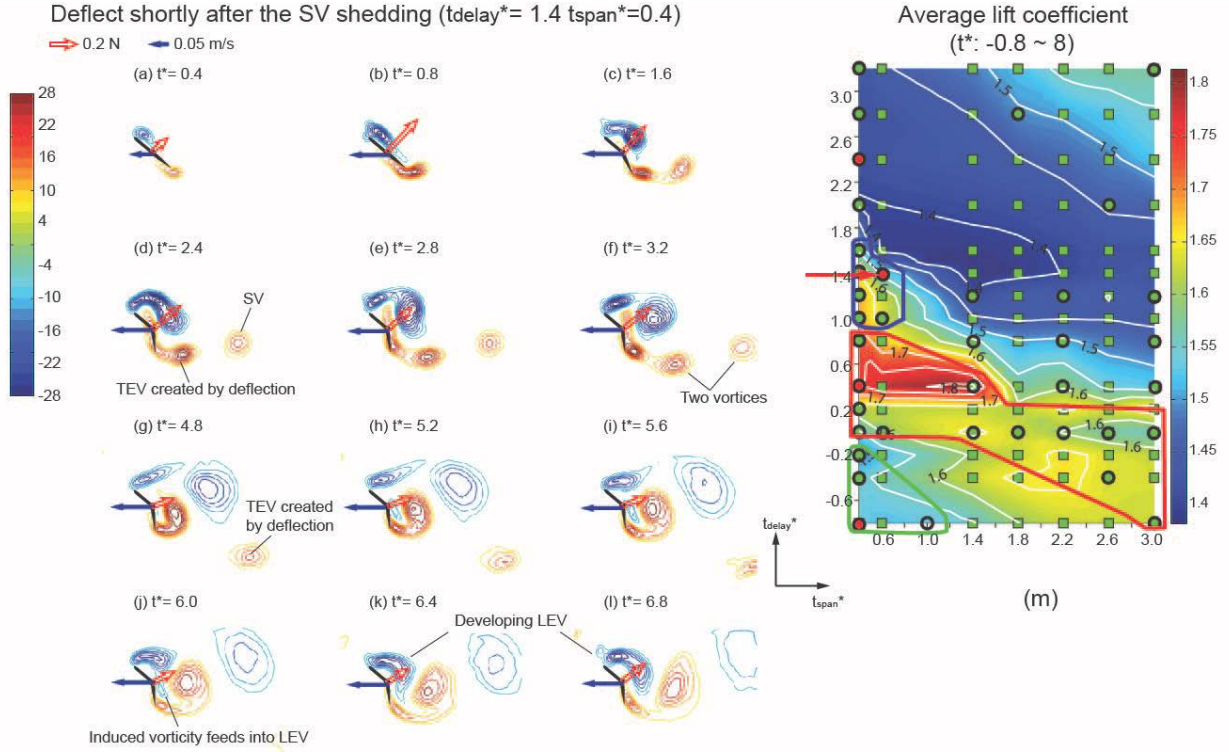
Figure 6. A typical flow in region III at tdelay*=1.4 and tspan*=0.8. (d) Another TEV was created by deflection beside SV. (j) Induced negative vorticity feeds into LEV.
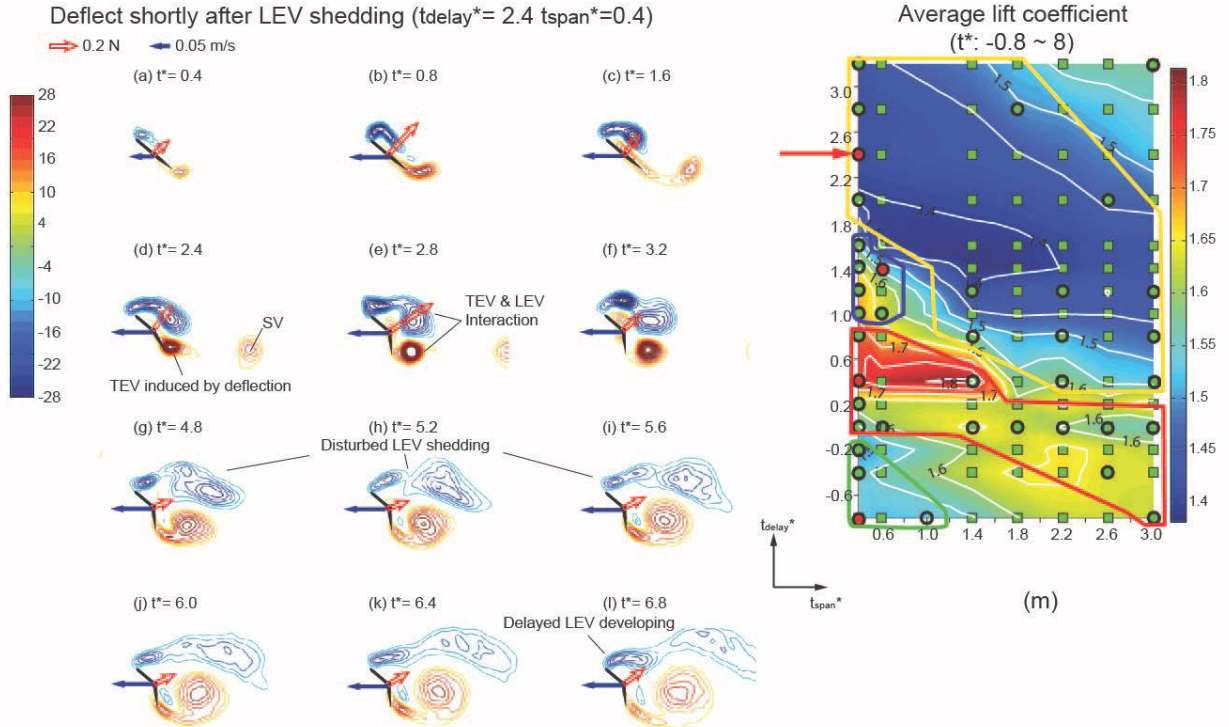
Figure 7. A typical flow in region III at tdelay*=1.4 and tspan*=0.8. (d) Another TEV was created by deflection beside SV. (j) Induced negative vorticity feeds into LEV.

14
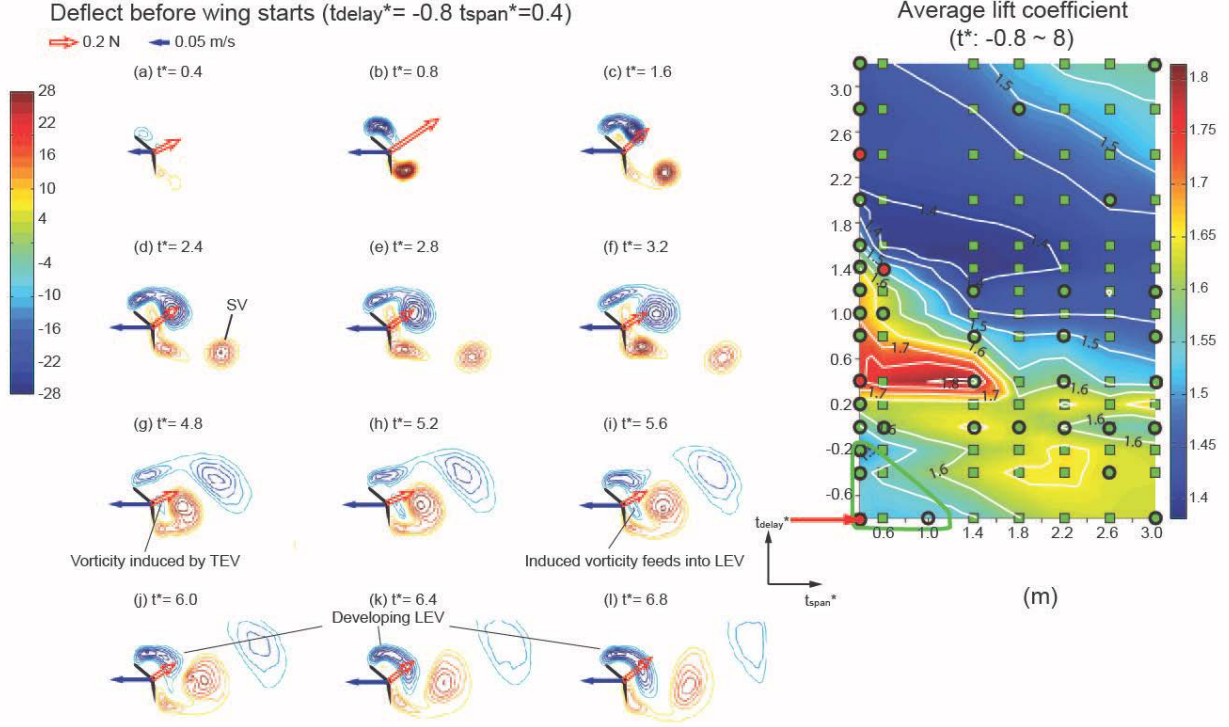
Figure 8. A typical flow in region I at tdelay* = -0.8 and tspan* = 0.4 where the wing deflects before the wing starts with a high deflection speed. (a-l) Contour plots of vorticity. Black parts present wing's cross section; Red empty arrows give the instantaneous net forces; Blue arrows show the translational velocity on the wing. (g) Negative vorticity was induced closed to hinge. (i) Induced negative vorticity feeds into LEV. (j-l) LEV is promoted by feeding the induced negative vorticity into LEV. (m) Region I highlighted by green loop. Red circle and arrow indicate where current contour plots of vorticity were measured.

Concluding Remarks:

The effects of timing and speed of active flap deflection were studied systematically using force and DPIV measurements. The results show that significant improvement on force performance can be achieved by a proper design of flap kinematics relative to the vortex shedding events. In particular, when the wing deflects slightly before the SV shedding with relatively fast speed, the wing produces maximum lift. However, if the wing deflects during or slightly after the LEV shedding, the lift is substantially reduced and close to that of the uncambered wing.

It is shown that by deflecting the flap within a certain range of timing at moderate speed, the vortex shedding on the wing changes dramatically and leads to four different patterns which can be directly related to four regions in the average lift contour plots. First, when the wing deflects before SV shedding, SV is enhanced by the deflection and a large lift peak is observed. Second, when the wing deflects between shedding of SV and LEV, a second TEV is shed in addition to the SV and a moderate average lift is observed. Third, when the flap deflects during or slightly after LEV shedding, it affects the shedding of LEV and delays the development of circulation, resulting in a low average lift due to the reduced LEV strength. Fourth, when the wing deflects before the onset of translation at a rapid rate, a low average lift is observed as the force and flow

15

structures are similar to those of the precambered wing. Therefore, there is an unequivocal strong correlation between the SV strength and lift production [34, 37].

To extend the current result to the 3D flapping wing case, the pronounced wing-wake interaction during the stroke reversal must be taken into account along with the effect of varying angles of attack throughout the stroke. Furthermore, in 3D flapping wings, because the tip and root vortices may play a critical role in defining the flow structure, the study of active wing morphing may do well to consider both the 3D and unsteady effects with both camber and twist wing design.

2.3 Understanding the flow physics of flapping/revolving wings

1) Understand dynamics of vorticity and vortices on revolving wing

In the first type of measurements, the near wake flow around a revolving wing was studied and the vorticity dynamics in the flow was particularly studied. The three dimensional velocity and vorticity fields were represented with respect to the base axes of rotating Cartesian reference frame, and the second invariant of the velocity gradient was evaluated and used as a criterion to identify the core of vortices. Two main vortex structures were found. The first vortex structure was a composite of leading, trailing and tip-edge vortices attached to the wing edges, whereas the second structure was a strong tip vortex tilted form leading-edge vortices and shed into the wake together with the vorticity generated at the tip-edge. Using the vorticity transportation equation, the convection, stretching, and tilting of vorticity in the rotating wing frame were evaluated. It was found that vorticity generated at the leading edge is mainly carried away by strong tangential flow into the wake and travels downwards with the induced downwash. The convection by spanwise flow is comparatively negligible. The three-dimensional flow in the wake also exhibits considerable vortex tilting and stretching.
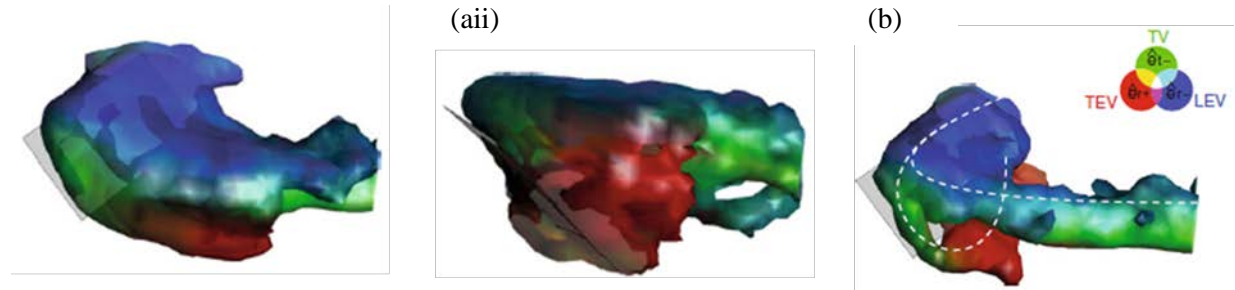
Figure 9. Isosurfaces of color coded vorticity magnitude and vortex structure. Vorticity magnitude viewed at two different angles. ai is looking down on the wing while aii is looking up on the wing. Isosurfaces are color-coded to reflect the direction of vorticity. RGB values of isosurface color correspond to magnitude of the vorticity components: trailing-edge vorticity red; leading edge vorticity, blue and tip voracity green. b vortex structure evalued by the isosurfaec of Q value.
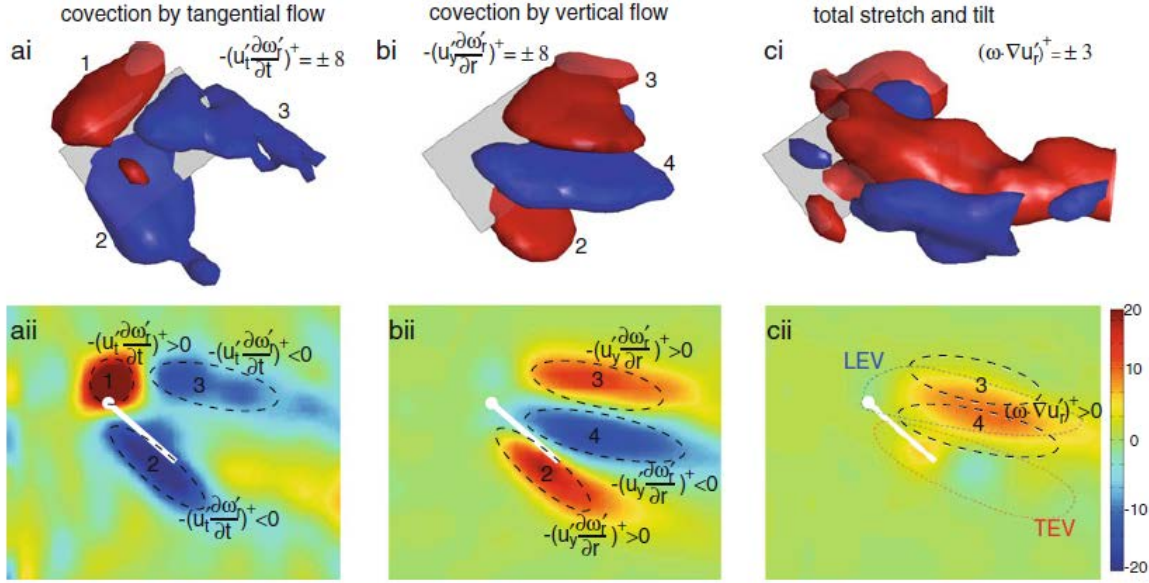
Figure 10. Isosurfaces of individual terms in vorticity equation (ai, bi,ci) and corresponding cylindrical slices at 75 % of wing span (aii, bii,cii). The isosurfaces in a and b are shown at dimensionless value 8, and that in c is shown at dimensionless value3. Regions 1, 2, 3 and 4 are indicated in both isosurfaces and cylindrical slices. In cii, the locations for LEV and TEV are also plotted

To identify specific vortex structures, we plotted the total vorticity magnitude isosurfaces with RGB colors indicating the vorticity direction (Figure 9). Based on the Q-value criteria for these flows, we identified the two major vortex structures on the wing (Fig 9b) which include the leading edge and trailing edge vortices and the tip vortex. The top structure consists of a combination of negative radial (LEV, blue) and negative tangential (TV, green) vorticity and extends into the wake (Figure 9a). The bottom structure consists of positive radial (TEV, red) and positive tangential vorticity (representative color not shown in Figure 9a). The top and bottom vortex structures connect at wing tip and form a horseshoe-like structure that is attached to the wing. From the top portion of this structure, a long tube-like tip vortex structure extends tangentially into the wake. At the relatively low Reynolds number of 220, these vortex structures are coherent and stable, and do not disintegrate, unlike similar structures at higher Reynolds numbers. The horseshoe vortex structure (Figure 9b) likely influences the observed tangential flow (Figure 9b) in the wing wake; while the arc formed by LEV and TV core (Figure 9b) likely influences the downwash .

To investigate the radial vorticity dynamics (LEV and TEV) in the wing rotating frame, and its effect on the stability of the vortex structures, we calculated and compared the individual terms of convection, stretching/tilting and diffusion. First, we found that the contribution of the convection along tangential and vertical direction to the vorticity change (Figure 10a, b) is significant. In comparison, the contribution due to convection by spanwise flow is quite low and may be neglected as it is even smaller than the diffusion term. Together, these observations suggest that the convection by tangential flow carries away the negative radial vorticity generated at the leading edge and convects it into a region behind the wing. In contrast, the downwash convects the vorticity out from this region, but brings it into a region between the LEV and the TEV vortex. Because the positive radial vorticity (TEV) is convected into region 2

17

by the downwash and away from the wing by tangential flow, the net vorticity in this region remains mostly unaltered.

Concluding Remarks:

We studied the velocity and vorticity fields generated by a revolving wing and evaluated the vorticity equation to interpret the vorticity dynamics. The results suggest strong three-dimensional phenomena of the flow, as there exists substantial vortex tilting and stretching. As one of the results, part of the radial vorticity is tilted into tangential vorticity, and shed into the wake. By comparing different terms in the vorticity equation, we found convection in tangential and vertical directions are responsible for a majority of the vorticity change, where those in the spanwise direction are negligible. In comparison, vortex tilting and stretching have a smaller effect than convection, but reduce the radial vorticity accumulated by vertical convection in a particular region [35].

 2) *Discover a possible universal flow feature on the hovering wings*

In the second type of flow measurements, we extended our flow measurement to the overall wake structure on the hovering wings. Totally, two volumetric flow measurements were performed on two mechanical flappers with different wing kinematics but similar wing geometry. On the flappers with small stroke angle and passive rotation, the general vortex wake structure maintains a quite consistent form: vortex rings in the near field and two shear layers in the far field. Vortex rings shed periodically form the wings and are linked to each other in successive strokes. In the far field, the shed vortex rings evolves into two parallel shear layers with dominant vorticity convected from tip and root vortices (Figure 11) [33].

On the flappers with large stroke angle and active wing rotation, however, no vortex rings were captured in the near wake but replaced by an integral vortex structure consisting of a tip vortex (TV), trailing-edge shear layer (TESL) and leading-edge vortex (LEV) (Figure 12, 13). In the far wake, very surprisingly, the flow structure on these two flappers in the far wake are quite similar in nature and dominated by two flat (small stroke angle) or curved parallel shear layers which are formed by the convection of tip and root vortices. Considering big differences exists in wing kinematics and Reynolds numbers between two experiments, we believe this tip and root vortices direct downwash in the far wake is a universal phenomenon on hovering wings and it might be related to the lift performance of the hovering animals [36].

Concluding Remarks:

The aerodynamics of flapping wings are characterized by the unique system of vortices shed in the wake, the structure and evolution of which reflect the wing morphology and kinematics. While the near-wake vortex system directly reflects the action of the wing on the fluid, the far-wake vortex pattern is under the influence of vortex interactions and viscous dissipation. It has been shown that the flapping wing model creates a series of complex vortex structures, and the overall effect of the wing motion is to deposit a vortex sheet (TESL combined with TV) into the wake, which contains vorticity components in all three directions (radial, tangential and vertical).
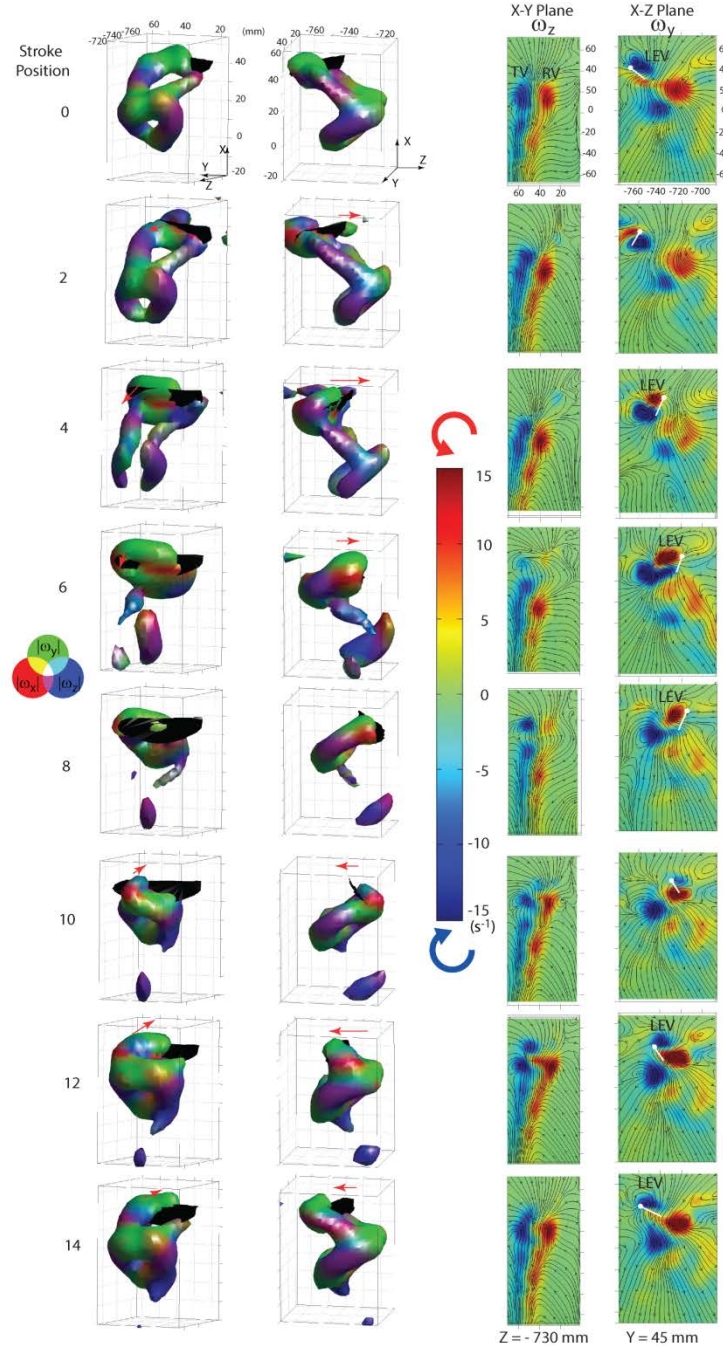
Figure 11. Isosurfaces of vorticity magnitude (|ω|= 10/s) and vorticity contour plots at 8 different stroke positions, which demonstrate the evolution of the vortex wake structure. The contour plot of Z vorticity at X-Y plane (Z = -730 mm) shows the tip vortex (TV) and root vortex (RV) as well as two shear layers in the far field. The contour plot of Y vorticity at X-Z plane (Y= 45mm) shows the leading edge vortex (LEV) and other vortices shed at stroke reversals.

19
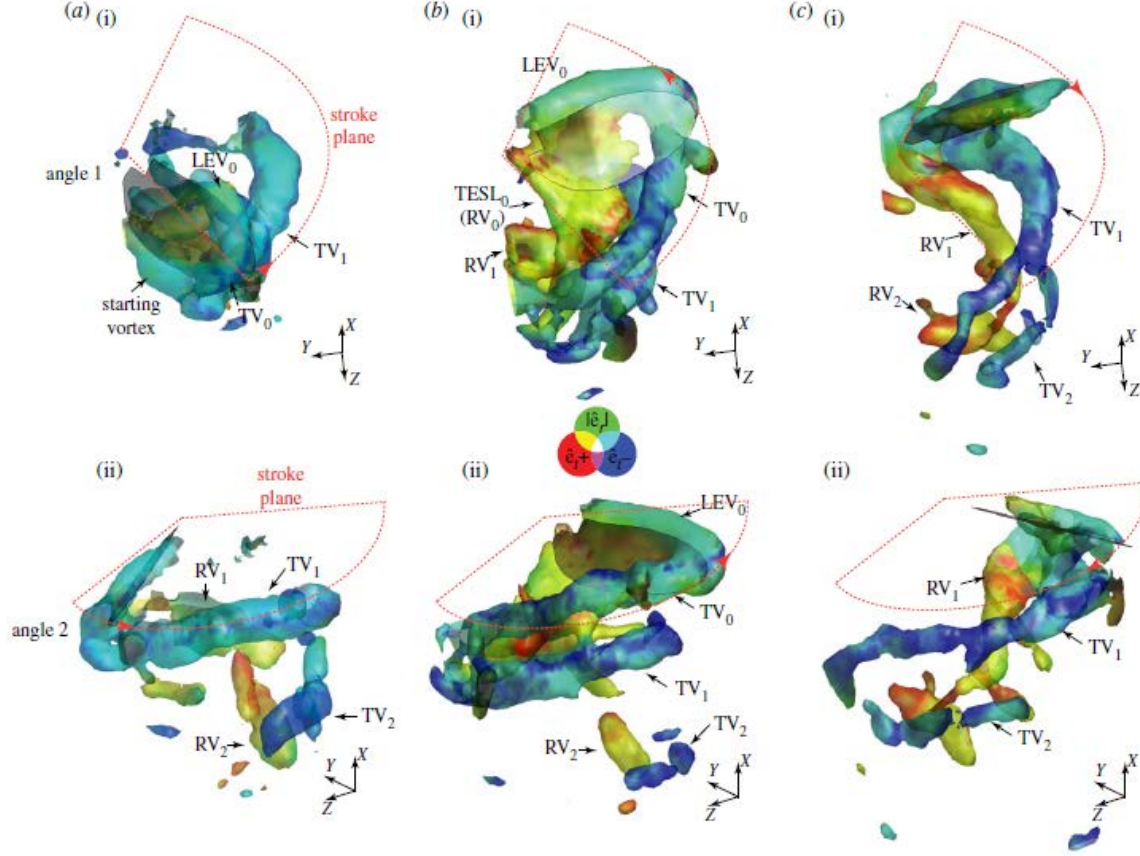
Figure 12. Colour-coded isosurfaces of vortex wake structure defined by Q = 0.25 at T = 0.1 (a), 0.3 (b) and 0.7 (c) viewed at two different angles (i) and (ii). RGB values of the isosurface colour correspond to the vorticity components: root vorticity, red; tip vorticity, blue; magnitude of radial vorticity, green. The TV, RV and LEV are labelled. Subscripts 0, 1, 2 denote vortices created by different strokes with larger numbers representing earlier strokes.
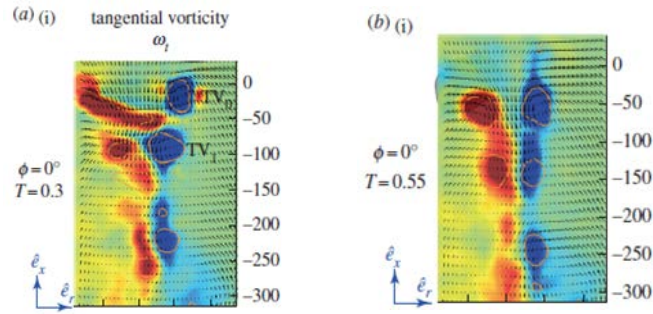
Figure 13. Contour plots of tangential vorticity on span-wise Slice. Contours of Q = 0.05 are superimposed to show the vortex structure. It shows clearly the downwash is directed and confined by the tip and root voritices.

3) *Smoke and dye visualizations on the hovering wings*

To observe and study the unsteady 3 dimensional flow on the flapping wings different visualization methods were tried and developed. Conventionally, the smoke wire visualization is used in wind tunnels which provide uniform and low turbulent free streams. Under this restriction, all the previous experiments of smoke wire visualization on flapping wings were performed in wind tunnels with nonzero free stream velocity which however could not provide an ideal hovering flight condition. Under the frame of this project we introduced and tested a new visualization technique on hovering insect wings. By placing the smoke wire close to the flapping wing, we expect the downwash to drag the smoke particles into the wake and to form smoke patterns that visualize the flow structure generated by the flapping wings. Figure. 14 shows the smoke visualization results for the flapping frequency at 5Hz, six frames for an upstroke (0-100ms) are shown, and three frames at 0, 40 and 100ms are shown in Figure 14b-d with more details. During the downstroke, a large downwash accompanied by a strong vortex at wing tip and a minor vortex at wing base were observed (Figure 14b). At the beginning of the upstroke, after the wing quickly rotating, the wing interacted with the wake of the down-stroke and two spiral rotational flow structures were observed (Fig 14c). At the end of the upstroke, a large downwash with a strong vortex pair at wing tip and base were observed (Figure 14d) [32].
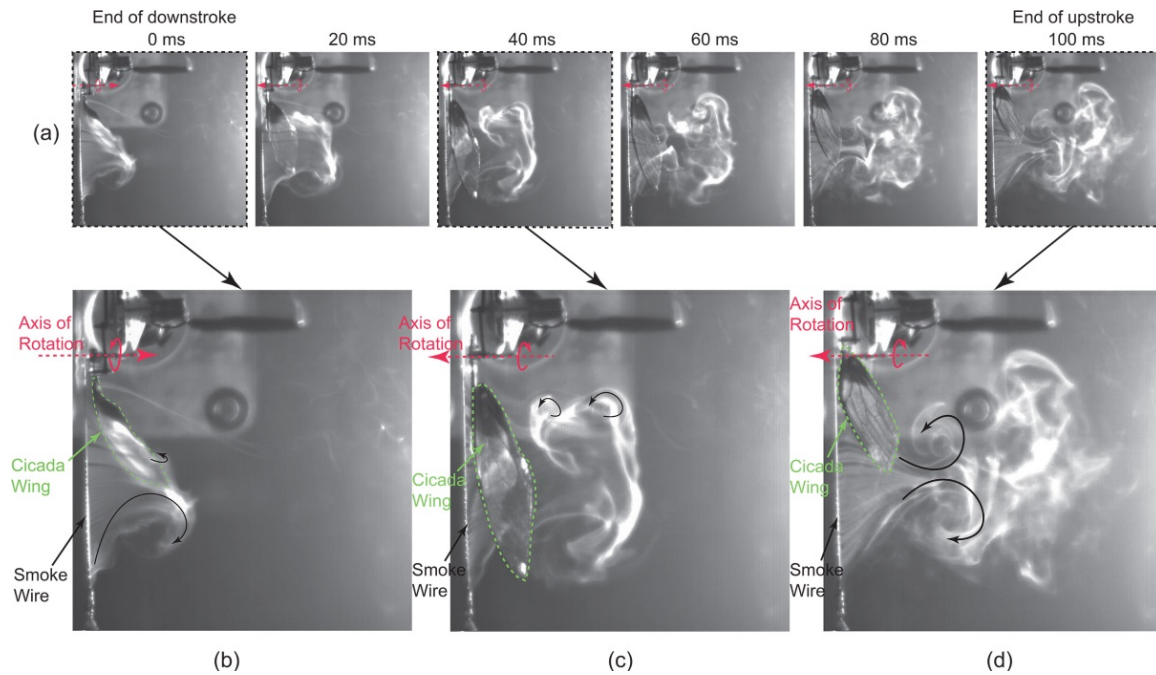
Figure 14. Smoke patterns showing the evolution of the flow structure in an upstroke (5 Hz). Downwash is confined in by tip and root vortices

3. Computation study

In this part, three sections regarding the numerical study on the proposed topic are presented. We briefly summarize these works in the following.

(1) Validation
- ➢ Simulation of a 2D flapping plate is validated by comparing our results with previous literatures [8,9].
- ➢ Numerical results (conducted by Co-PI's group) of a 3D translational plate are compared with experimental results (conducted by PI's group) in both the aerodynamic performance and the vortex formation. It is found that the numerical results and the experimental results agree well with each other.
- ➢ Comparison between the simulation of a 3D rotational plate and previous experimental results [10] is conducted to further validate our numerical method.

(2) Trailing control in stationary and flapping plates
- ➢ The investigation of flow pass 2D stationary deformed plates reveal that both aerodynamic performance and vortical structures could be modified according the camber magnitude and camber formation timing via a trailing-edge flap (TEF). This finding inspires us to further pursue the effects of trailing-edge flap in flapping flight.
- ➢ A model of 2D flapping plate with dynamic trailing edge deviation is built. Two adjustable parameters trailing-edge deflection amplitude and phase shift are used to control the trailing edge flap. Parametric study shows that: 1) TEF phase shift play a dominant role in force production and flow modulation. 2) Purely changing the deflection amplitude will not change the overall aerodynamic characteristics. 3) Lift enhancement by applying TEF is from the change of local circulation. 4) The vortex structure on the suction side is pulled down closer to the plate and this leads to a larger range of low pressures field. This change will further modulate vortex shedding process and creates a more persistent jet in vertical direction.
- ➢ Unsteady aerodynamic performance of deformed flapping plated has also been considered for three-dimensional flows. Through applying different trailing-edge shape, the surface pressure distribution on the suction side will be changed and result in a vortex structure modulation.

(3) Understanding the flow physics of flapping/revolving plates
- ➢ Passively deformable flapping wings are modeled as a hovering rigid membrane plate with a torsional spring placed at the leading edge and driven sinusoidally with the deflection of the membrane determined by its interaction with the surrounding fluid. The effects of hinge stiffness and stroke amplitude are studied and aerodynamic performance is discussed in detail.
- ➢ Two types of hinged plate in hovering, i.e., 1) one-link plate with free-to-pivot hinge at the leading edge and 2) two-link plate with a free-to-pivot hinge at the lower link, are studied to explore the effects of the flexibility of flapping wings. It is found that the benefits of chord-wise flexibility can only obtained when the hinge location is carefully

selected. It is a tradeoff between the lift sacrifice and drag reduction, which are two effects simultaneously brought in the game by the flexibility.

➢ Direct numerical simulation (DNS) is used to study three-dimensional flow structures and aerodynamic performance of varying aspect ratio revolving plates in fixed tip Reynolds number. We found that the larger aspect ratio cases present more unstable vortex formation and much stronger wing-wake/wake-wake interactions.

➢ The symmetry property and corresponding virtual force contribution of the proper orthogonal decomposition (POD) modes are numerically investigated for the flows generated by a low-aspect-ratio plate undergoing a pitching-plunging motion. It is found that the flow and its POD modes have the same reflectional symmetry about the spanwise central plane and half-period symmetry about the crossflow central plane. The POD modes are classified into two categories of thrust and lift producing, which can be used to identify the correlation between the wake structure and the hydrodynamic force generation.

4.1 Validations

1) 2-D validation of flapping plate

The simulation of the unsteady flow around a thin and rigid plate is compared with previous results [8,9]. In this test, the wing rotates around its center, whose orientation is measured counterclockwise relative to the positive x-axis and the amplitude is denoted by β. for the main plate kinematics. To match the simulation setup, $A_0/c = 2.8$ and $\beta = \pi/4$ are chosen for the wing kinematics and the Reynolds number, based on U_{max} and c, is 75. The flow is initially quiescent. The lift and drag coefficients for first a few cycles are shown in Figure 15. It can be seen that the present simulation has very good agreement with both experimental measurements [8] and numerical results [9] where a viscous vortex particle method (VVPM) was used.

In Figure 16 we present the wake development by showing the vorticity field at different time instants. The corresponding flow field from [9] is shown for comparison. It can be seen that the instantaneous vortex structures from the two simulations agree with each other very well.

2) 3-D validations of plates in translational motion

In order to demonstrate the validity of the numerical code, we compare our simulation results with experimental measurements. Results from the three-dimensional simulations were compared with measurements from an oil tank experiment of flows over a rectangular plate of dimension 80mm $\times$160mm $\times$3mm (AR=2). The temperature in the laboratory is regulated at $20 \pm 1\,°C$ ℃ such that there is less than 3% variation in the kinematic viscosity ($12 \pm 2cSt$). The rectangular flat plate at different angles of attack were accelerated and reached to its maximum velocity after 0.5 seconds. The Reynolds number in current study is fixed at 495. The comparison of flow structures and force history are presented in Figure 17 (a) and (b), respectively. We can see that both the flow structures and the performances of the plate show very good agreements. The time of maximum lift appeared at t ≈ 0.3 ≈0.3, which results from the inertial force during impulsive start process.
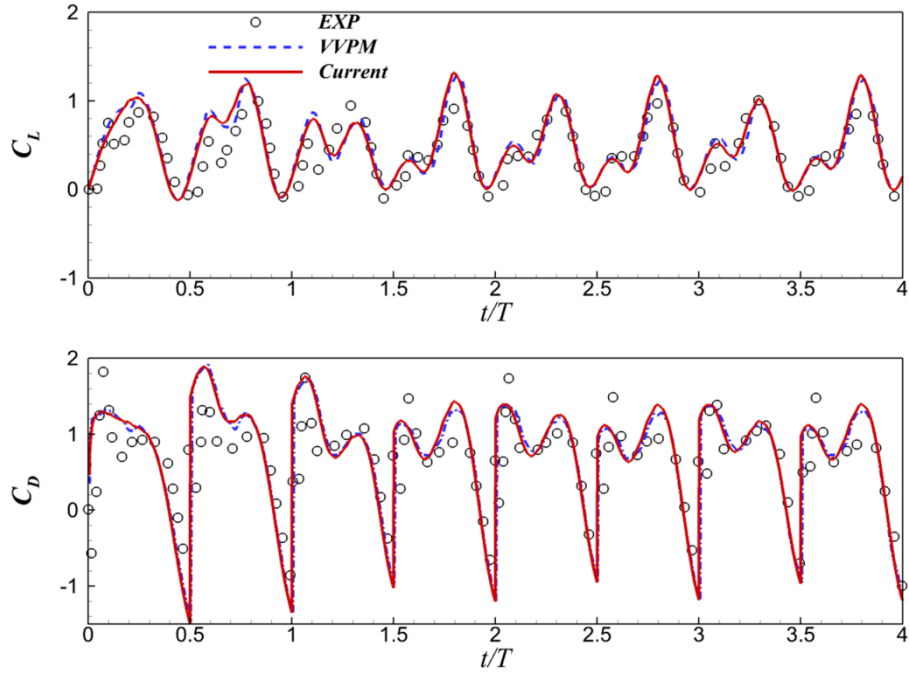
Figure 15. Lift and drag coefficients from the current simulation (red solid line), from experimental measurement (black dashed line) [8] and from VVPM simulation (blue dash-dot line) [9].

| $t/T=3$ | $t/T=3.25$ | $t/T=3.5$ | $t/T=3.75$ | $t/T=4.0$ |
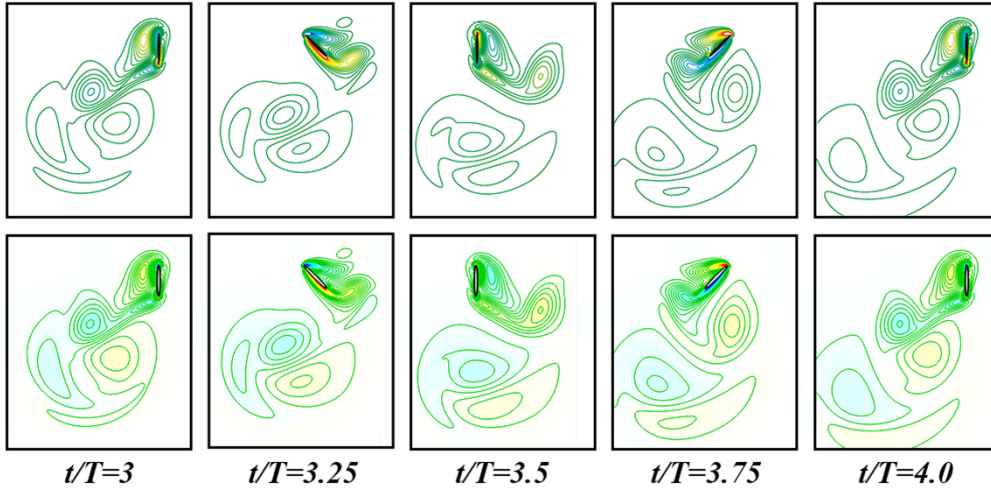
Figure 16. Vorticity field at the labeled instants with 40 contour levels distributed uniformly between -20 and 20. The top row is from [9], and the bottom row from the current simulation.

3) 3-D validation of plate in rotational motion

For the third validation case, rotational experiment [10] was performed in an 18in×18in×18in glass tank filled with mixing water/glycerin. The geometry considered in this
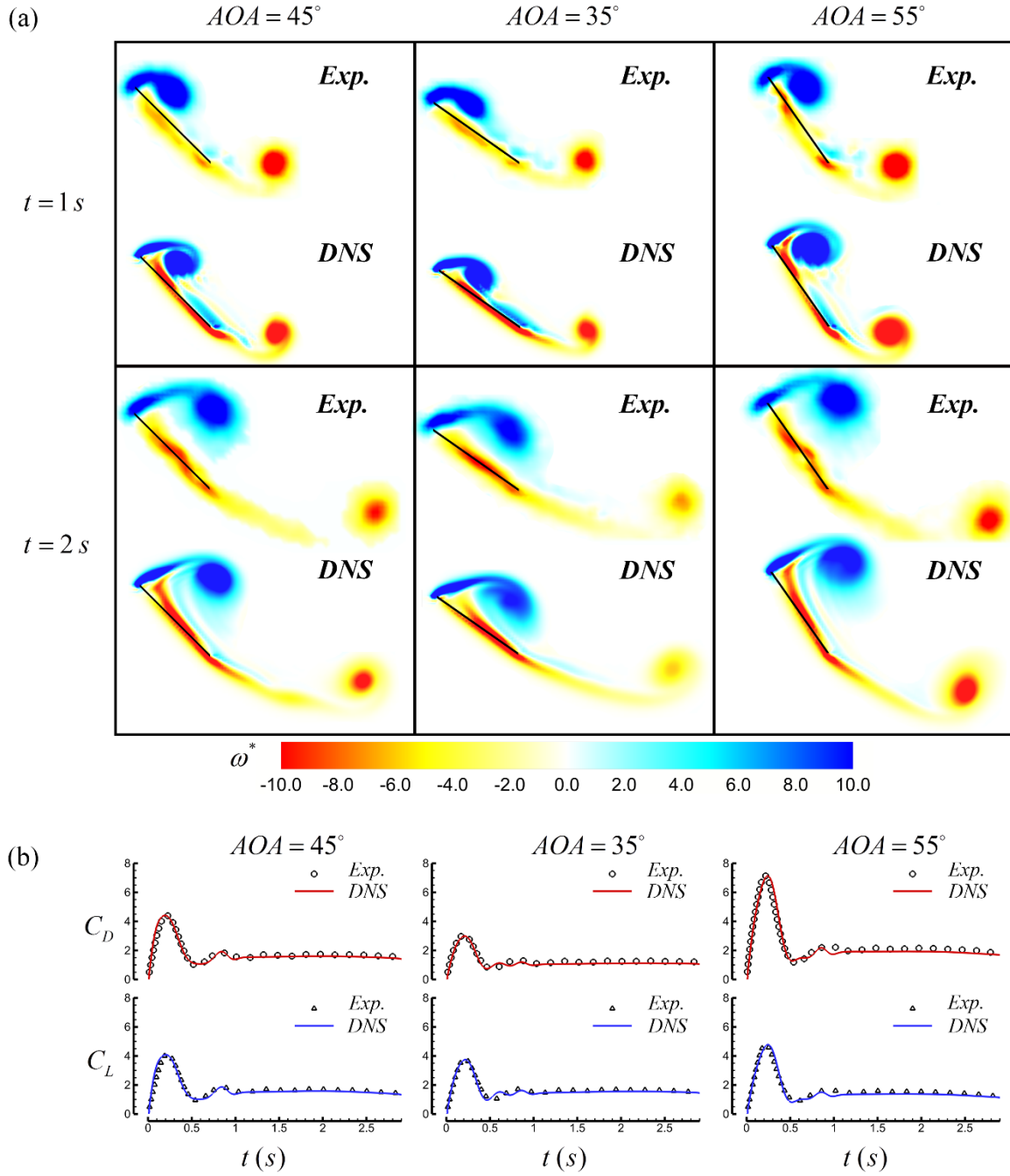
Figure 17. Validations between experimental measurements and direct numerical simulations for rectangular plate (AR=2) in translational motion at Re=800, and $\alpha = 35°, 45°$ AOA = **45°, 35°** and **55°**. (a): spanwise vorticity contours of slice cut of flow fields at 50% chord; (b) time history of drag and lift coefficients.

study is an aspect-ratio-two rectangular wing. The root of the wing is extended out a distance of r=0.5c from the rotation axis at a fixed angle of attack 45°. The wing is initially at rest in quiescent flow before accelerating to a constant rotational rate as it revolves around its axis, and the total rotational angle is 720°. The velocity profile used for the experiments consists of a

piecewise linear function in three phases: an acceleration phase, a constant speed phase, and a deceleration phase. The acceleration and deceleration were chosen so that the speed increases linearly over 0.25c of travel at 75% of tip radius.

The Reynolds number for this case equals to 500. Lift coefficient time-histories are shown in Figure 18. For the case with 0.25c acceleration duration, the lift coefficients experienced a sharp peak associated with the inertial forces, followed shortly by a second peak. The simulation results for this case also have a good agreement with the experimental measurement.
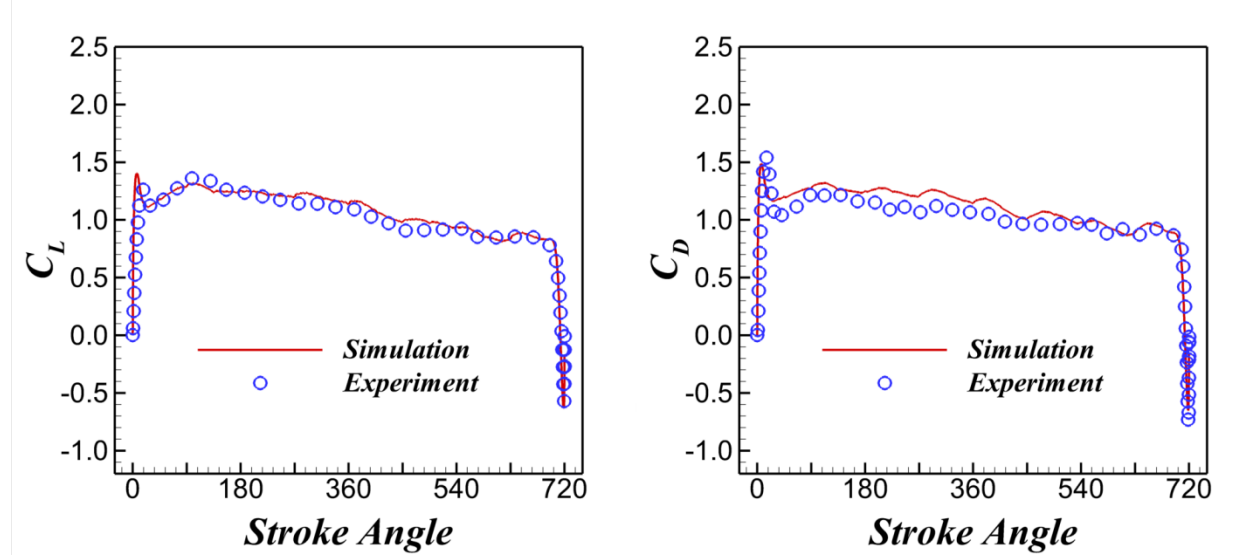
Figure 18. Time history of lift and drag coefficients for rectangular plan-form (*AR*=2) in rotational motion at Re=500, and $\alpha = 45^{\circ}$. (A) Comparison of Lift coefficient; (B) Comparison of Drag coefficient.

Concluding Remarks:
The in-house flow solver is validated though a sets of validation cases. The flow structures and force histories are compared between experimental measurements and DNS results. The results show very good agreements.

4.2   Trailing edge control of stationary/flapping plate

1) Flow pass deformed plates

The aerodynamic performance of 2-D flow pass stationary cambered plates are investigated. For stationary cases, the hinge location at 75% chord distance from the leading-edge can generate higher lift compare to rigid plate. Different value of the hinge location (HL) and trailing-edge deflection angle are numerically investigated. The computational setup is shown in Figure 19(a). From the polar plot of lift and drag coefficients (Figure 19(b)) we observed that the hinge location at three quarter chord distance from the leading-edge can improve the lift production and shows the monotone increasing.
2) Flow pass plates with dynamic trailing-edge flap motion

For examining the effect of trailing-edge flap, flow pass stationary plate (AoA=45°) with dynamic trailing-edge deflection motion are investigated. For fully rigid plate, von Kaman Vortex Street is developed when flow reaches to a quasi-steady state with vortex shedding frequency f_v, as shown in Figure 20(a). This vortex shedding pattern can be change to different pattern when the trailing-edge flap deflect at 4 times f_v, as shown in Figure 20(b-d). For up-stream deflection motion, the leading-edge vortex (LEV) is enhanced, as shown in Figure 20(c), and LEV is much closer to the suction side of plate comparing to the fully rigid one. On the contrary, the phenomenon of down-stream deflection is preventing the development of LEV.
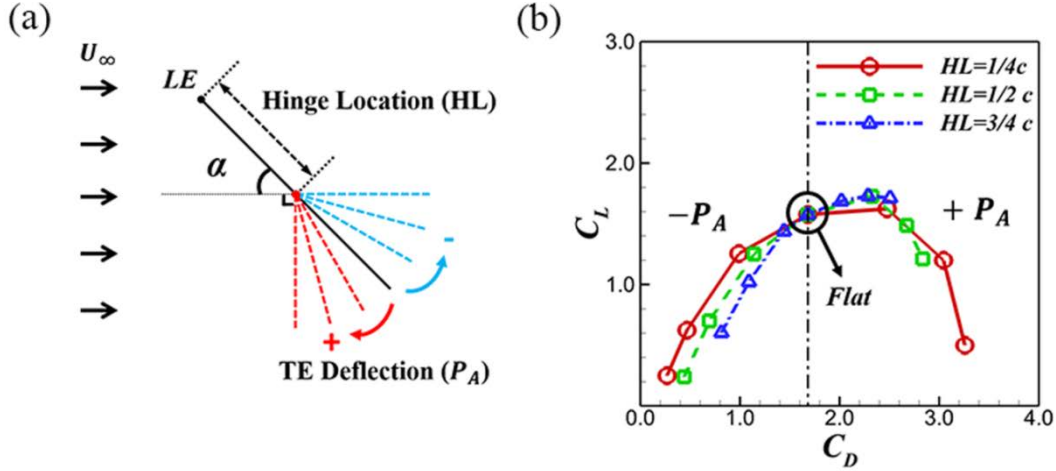
Figure 19. (a) Flow pass stationary cambered plate at different trailing-edge deflection angle and hinge location; (b) Polar plot of lift and drag coefficients at various hinge locations.
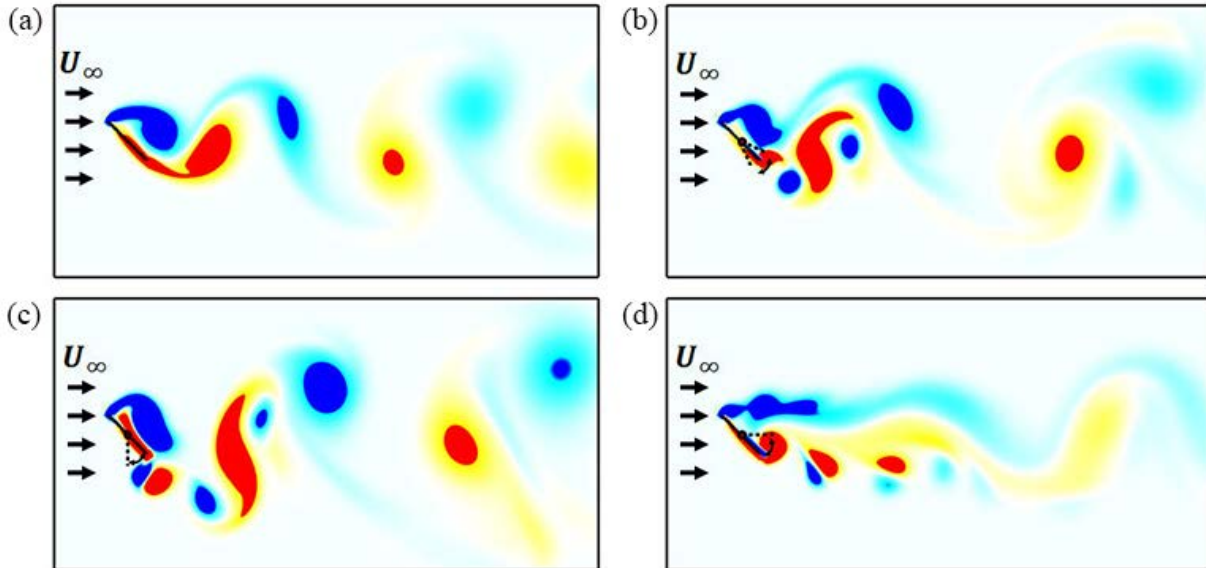
Figure 20. Vortex shedding behind a membrane plate which has 45° angle of attack (a) fully rigid plate; (b) symmetry deflection; (c) up-stream deflection; and (d) down-stream deflection.

3) Effects of a controllable trailing-edge flap on hovering plate

For examining the effect of wing-morphing on unsteady aerodynamics, a 2D deformable flapping plate by attaching a trailing-edge flap (TEF) is investigated numerically in the low Reynolds number regime. Current work focuses primarily on steady hovering motion with different types of TEF deflection pattern. Geometrically, the TEF deflection directly results in a variety of dynamic camber pattern when the deflection amplitude and phase shift are justified. Results show that the phase shift between leading-edge rotation and trailing-edge deflection dominates the aerodynamics of the flapping plate. A moderate deflection amplitude can only optimize the performance when a suitable phase shift value is chosen. Further analysis illuminates that an effective TEF deflection motion can feed extra circulation into the trailing-edge vortex and thus enhances the strength of its pair leading-edge vortex. This local circulation change will further influence the whole vortex shedding process and creates a stronger persistent jet in vertical direction. By tailoring the TEF deflection amplitude and phase shift, the overall lift can be enhanced up to 26% comparing to a fully rigid plate. The present work is done through an in-house immersed boundary method based Direct Numerical Simulation (DNS) solver. Results from current parametric studies will be used to analyze unsteady force productions due to dynamic camber formation in flapping flight.
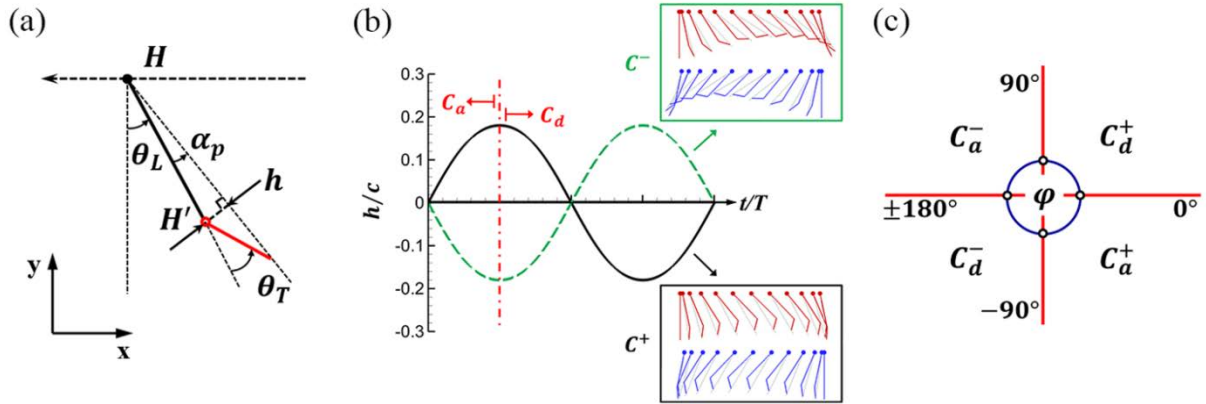
Figure 21. (a) Conceptual illustrations of plate deformation along with the definition of the maximum camber height, h, and local prescribed pitching angle, α_p; (b) Definition of advanced (C_a), delayed (C_d), positive (C^+) and negative (C^-) camber formation. The configuration shown in black and green box is corresponding to $\varphi = 0°$ and $\varphi = 180°$, respectively, at $\beta_T = 60°$; (c) Categories of camber formation for different range of phase shift (φ).

In current study, the main varying parameters to control the plate deformation are trailing-edge deflection amplitude (β_T) and phase shift (φ). By increasing β_T from $15°$ to $90°$, the maximum camber-to-chord ratio (h_{max} / c) will change from 4.9% to 23.7%. In other words, purely varying β_T will results in the change for camber magnitude. Unlike deflection amplitude, the variation of φ will lead to the change of camber timing. According to φ changing between $-180°$ to $180°$,
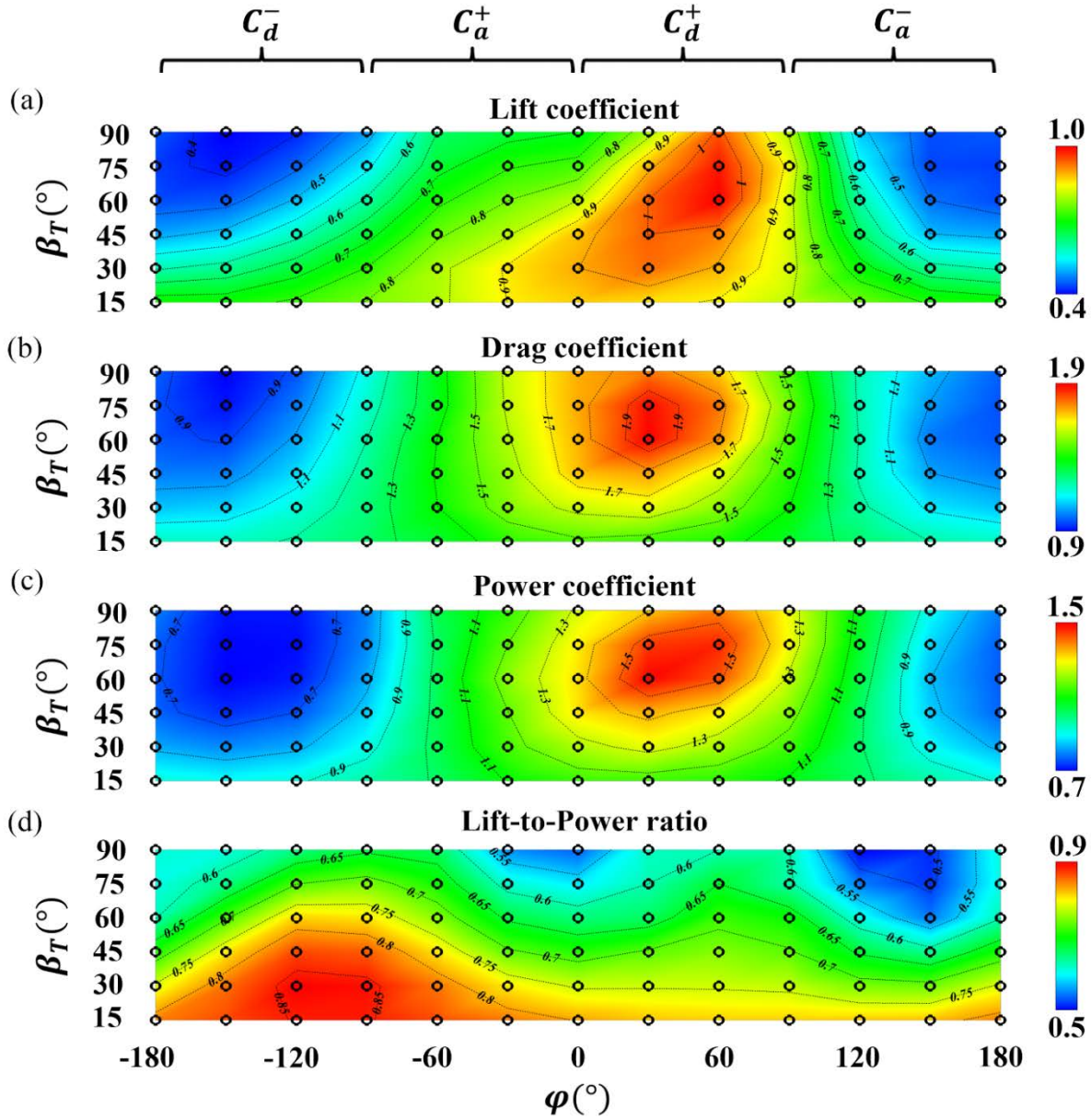
Figure 22. Parameter maps of mean lift (a), drag (b), and power (c) coefficients, and lift-to-power ratio (d) as a function of TEF deflection amplitude (β_T) and phase shift (φ).

the camber pattern can be further categorized as different typical groups. These categories are identified based on two features. One is the relative camber arch shape which can be either positive or negative during flapping. Another one is based on the camber peak appearance timing which can either shift to the first half or the second half of each stroke. Specifically, if the camber arch shape always towards the translational direction during the majority (more than half) of each down-stroke, we present it as positive camber formation (C^+). Oppositely, it will be denoted by C^- representing the negative camber formation. One selected example for each, corresponding to $\varphi = 0°$ and $\varphi = \pm180°$ at $\beta_T = 60°$, is shown in black and green box (Figure 21b), respectively. Note that, for these specific cases, the maximum camber is always formed at the middle of each stroke. However, when φ is changing in the range of $(0°, \pm180°)$, the camber peak
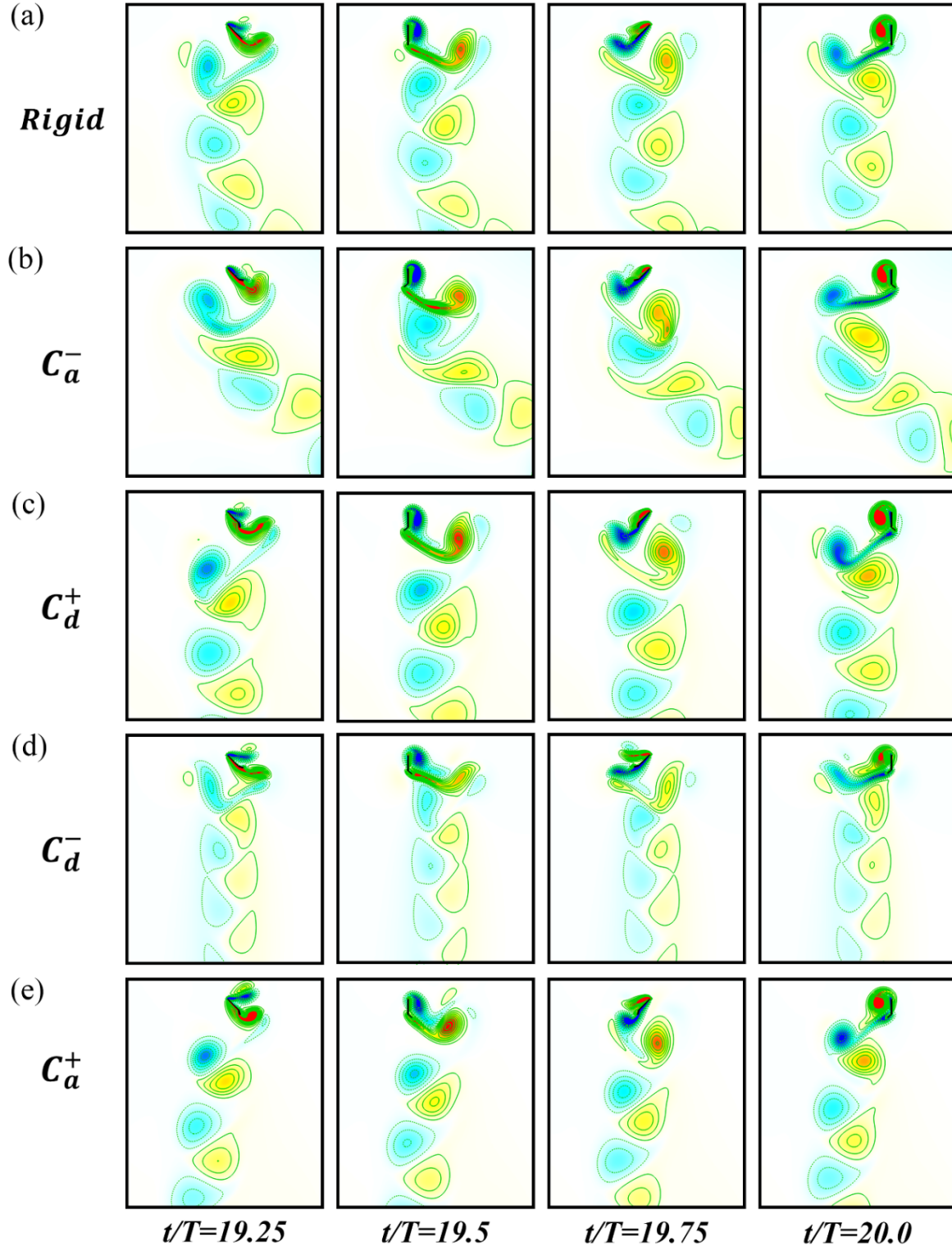
Figure 23. Vorticity field at the labeled instants. (a) Fully rigid plate; (b-e) Plate with TEF at same deflection amplitude ($\beta_T = 60°$) and different phase shift value $\varphi = 120°$ (b), $\varphi = 60°$ (c), $\varphi = -120°$ (d), and $\varphi = -60°$ (e).

will be either advanced or delayed. If the maximum camber appears during the first half stroke, we call it as camber with advanced peak, which is denoted as C_a. Otherwise, it is represented as C_d representing camber with delayed peak. Thus, four coherent regions are identified for $\varphi = (0°, \pm180°)$, as shown in Figure 21c: 1) positive camber with delayed peak (C_d^+); 2) negative camber with advanced peak (C_a^-); 3) negative camber with delayed peak (C_d^-); and 4) positive camber with advanced peak (C_a^+).

To provide a more comprehensive picture of how aerodynamic performance changes with plate kinematics, we further provide the performance contour for all pairs of TEF deflection amplitude, as shown in Figure 22. In general, there is no monotonous trend for any deflection amplitude. Which gives a broad maximum and minimum regions for each contour map.

In Figure 22a, lift coefficient map exhibits a broad maximum ranging from 0.9 to 1.06 between phase shifts of $0°$ and $90°$. This region is categorized as C_d^+, as aforementioned. Moreover, this also shows that for all deflection amplitude studied in current work, the delayed positive camber formation can always enhance the lift production comparing to the rigid case. The optimal configuration happens when $\beta_T = 60°$ and $\varphi = 60°$, which can achieve up to 26% lift enhancement comparing to rigid case. As expected, the drag (Figure 22b) also present higher value at this region. This is wildly happened for unsteady mechanisms. According to Wang [11], an increase in aerodynamic lift due to the unsteady effects is typically accompanied by an increased in drag [1,8].

The power coefficient contour map (Figure 22c) also displays a similar pattern as the drag coefficient. Unlike force and power coefficient map that higher value always appears at higher deflection amplitude, the lift-to-power ratio (Figure 22d) presents a relatively higher value at lower deflection amplitude, especially for $\beta_T = 15°$ and $30°$. This is caused that the frontal area of lower deflection amplitude cases will consume less power, and it makes the lift-to-power ratio rise up. This high lift-to-power ratio region is categorized as C_d^- in our early discussion. Another category which is defined as C_a^+ owns a moderate performance for both lift and lift-to-power
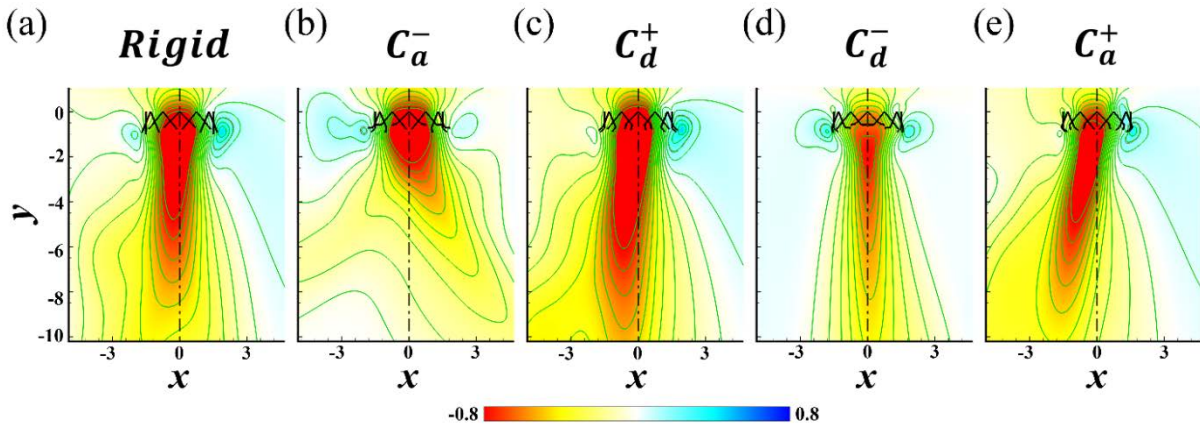
Figure 24. Contours of mean velocity (in vertical direction). (a) Fully rigid plate; (b-e) Plate with TEF at same deflection amplitude ($\beta_T = 60°$) and different phase shift value $\varphi = 120°$ (b), $\varphi = 60°$ (c), $\varphi = -120°$ (d), and $\varphi = -60°$ (e).

ratio comparing to those high lift and high efficient region. However, for the negative advance

camber formation (C_a^-), all aerodynamic characters show a lower performance neglecting the changing of deflection amplitude.

To show the global impact of camber formation, Figure 23 and Figure 24 presents the far field vortical structure and mean flow (in vertical direction) for different TEF kinematic pattern. After a long-term development, the far filed of flow present a reverse Karman vortex street. A vortex-induced jet can be seen from the mean flow. This flow feature was seen experimentally [12] and numerically [13] in hovering motion. The development of this persistent jet is a result of interaction between the reverse Karman vortex street and the downward momentum created by the translation of plate. As the plate passes the jet, vortices are shed with an orientation that reinforces the downward momentum previously created by the plate. Theses vortices sustain the downward momentum, and they further entrain surrounding fluid and interact with each other during subsequent stroke. Finally, this pocket of downward momentum takes the form of a persistent jet.

Concluding Remarks:

Parametric study shows that: 1) TEF phase shift play a dominant role in force production and flow modulation. The lift enhancement can only be achieved for a specific camber formation category which owns the positive camber with delayed peak (camber peak appears at the second half of each stroke); 2) A moderate deflection amplitude can only benefit aerodynamic performance in a suitable phase shift range. Purely changing the deflection amplitude will not change the overall aerodynamic characteristics. By tailoring the trailing-edge deflection angle and phase shift, the lift enhancement can reach up to 26% comparing to fully rigid flapping plate; 3) Lift enhancement by applying TEF is from the change of local circulation. It will feeds extra circulation to the TEV and thus induce a stronger pair LEV. As a consequence, the vortex structure on the suction side is pulled down closer to the plate and this leads to a larger range of low pressures field. Thus, the lift production is enhanced resulting from the increasing pressure difference. This change will further modulate vortex shedding process and creates a more persistent jet in vertical direction.

4) Effect of trailing-edge flap in three-dimensional hovering motion

Unsteady aerodynamic performance of deforming flapping plate has been considered for two-dimensional flows in last section. In this section, the performance exerted upon the plate as well as the 3D wake structures will be considered. Three-dimensional effects such as the aspect-ratio and the geometry of the trailing-edge flap will also be studied.

The model considered in this study is a zero thickness rectangular plate with varying aspect ratio. The root of the plate is extended out a distance of $r_{root} = 0.5c$ from the axis of rotation. The plate follows a sinusoidal sweeping and pitching motion in an idealized horizontal stroke plane. Since there is no deflection on the stroke plane, the trajectory of a rigid plate can be described by two degrees of freedom. One is the leading-edge position angle (Ψ) in spherical coordinates, and the other is the pitching angle (Θ). The plate motion is then specified by two periodic functions: $\Psi(t)$ and $\Theta(t)$. It is impractical to enumerate the whole family of kinematics by brute-force approach. The model chosen here is one of the simplest possible families of a hovering
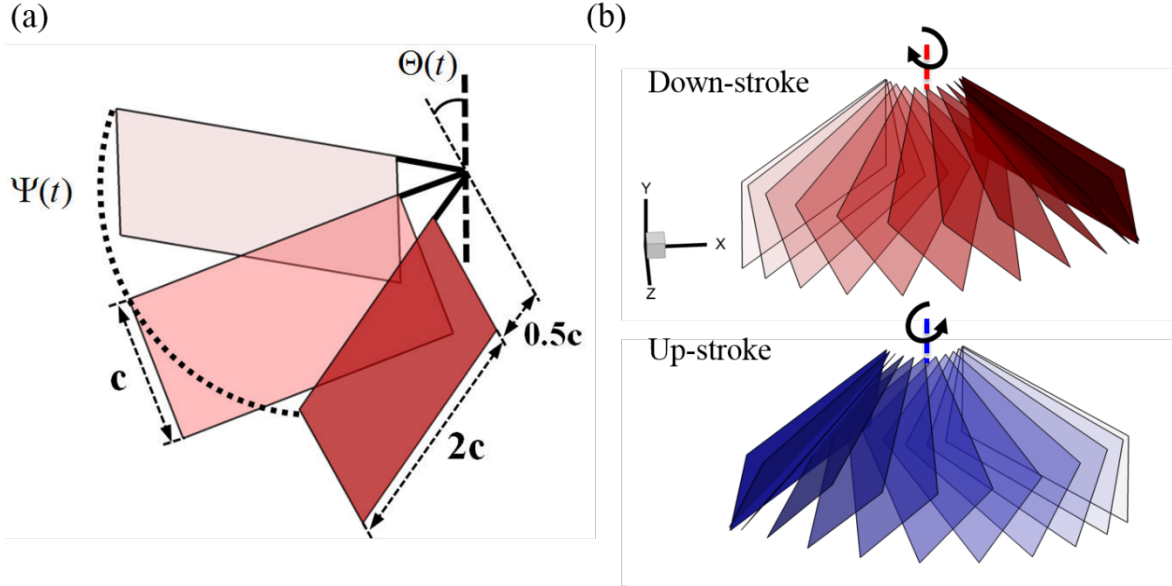
Figure 25. Three-dimensional flapping plate kinematics. (a): Plate geometry and definition of kinematics parameters; (b): Flapping plate configuration during down-stroke (red) and up-stroke (blue).

motion but it allows studying the dependence of the force and flow by applying dynamic trailing-edge flapping.

A trailing-edge flap, accounting for 25% of the total area of plate, is hinged on the plate with three different shapes, as shown in Figure 26. The same as previous two-dimensional study, the deflection angle (θ_T) of trailing-edge flap is prescribed with respect to the hinge axis for mimicking time-varying camber deformation in three-dimensional space.
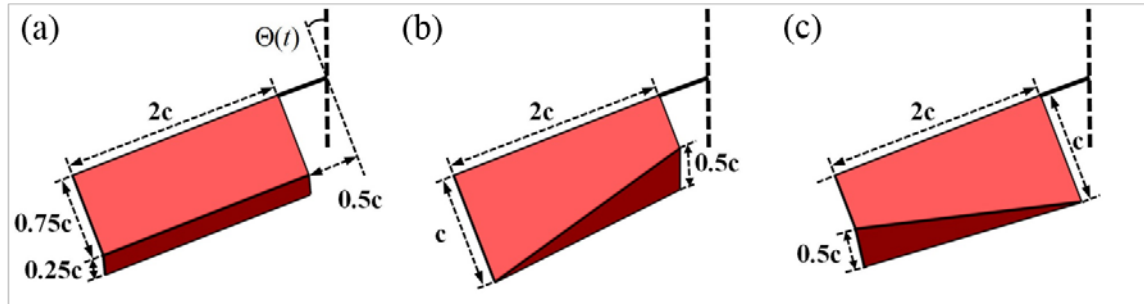
Figure 26. Three types of trailing-edge shape. (a) Rectangular shape (TS); (b) Left triangle shape (LTS); (c) Right triangle shape (RTS).

Error! Reference source not found. gives the time courses comparison of lift coefficient (C_L) and drag coefficient (C_D) of plates with different trailing-edge flap (TEF) shape in a completed third and fourth flapping cycles at a fixed Reynolds number 100. The instantaneous aerodynamic performance generated by the plate for different TEF shape cases share the similar tendency for drag coefficient but not for lift coefficient. Overall, in the current flow condition, both RS and RTS cases have relatively better performance in terms of lift production.

Figure 28 presents the comparison of surface pressure distribution on the suction surface of plate. By adding the trailing-edge flap, the whole surface pressure distribution was changed tremendous. The pressure on the suction surface becomes lower due to the presence of the trailing edge flap, especially in RTS case, which results in a higher lift correspondingly. From

the analysis of the flow structure, it is found the dynamic trailing-edge flap enhanced the leading-edge vortex and the tip vortex, which is responsible for the lift enhancement. The vortex structure of the fourth flapping cycle is shown in Figure 29.
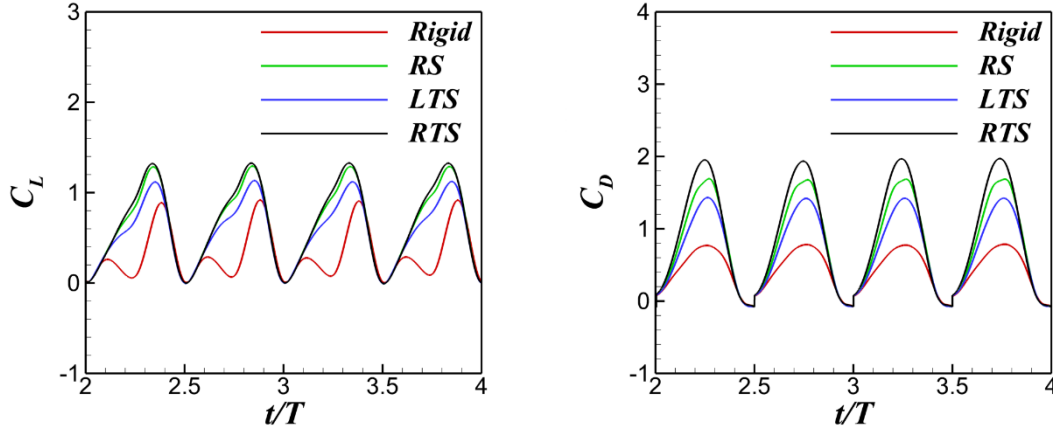
Figure 27. Comparison of instantaneous lift and drag coefficient for different trailing-edge shape (Rigid: without trailing-edge flap; RS: rectangular trailing-edge shape; LTS: left triangular trailing-edge shape: RTS: right triangular trailing-edge shape) during the third and fourth flapping cycle.
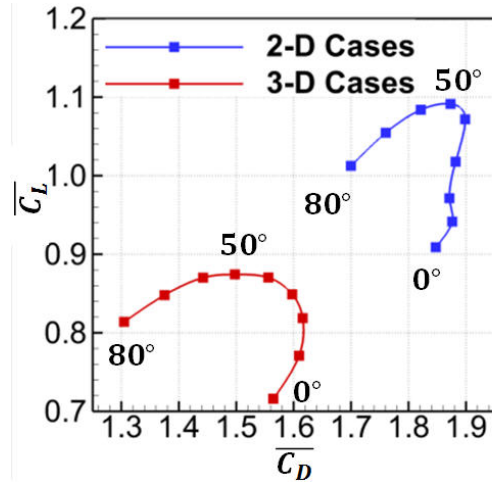
Figure 30. Polar plot of lift and drag coefficient for 2-D and 3-D cases at phase shift changing from 0 to 80 degrees.

Figure 30 shows the comparison between 2D and 3D aerodynamic performance by adding a trailing-edge flap. Generally, 3D flapping plates have lower lift coefficient amplitude compared to 2D cases. But for both 2D and 3D cases, maximum averaged lift coefficient happens at phase difference φ=50 degree in a given pitching amplitude.
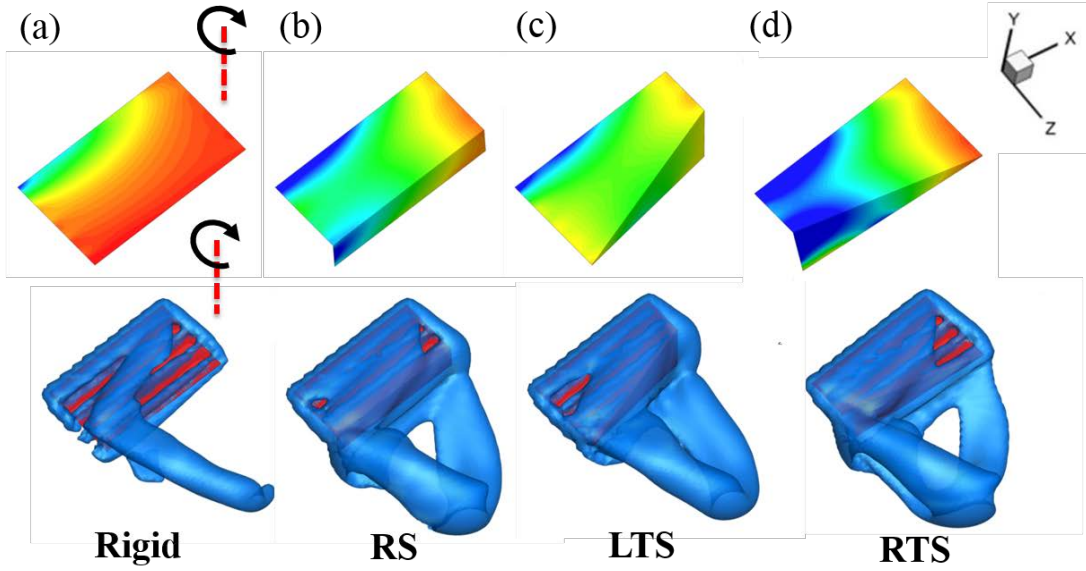
Figure 28. Comparison of surface pressure distribution on the suction side of the plate (A) and iso-surface vortex structure (B) for different trailing-edge shape at the middle of down-stroke
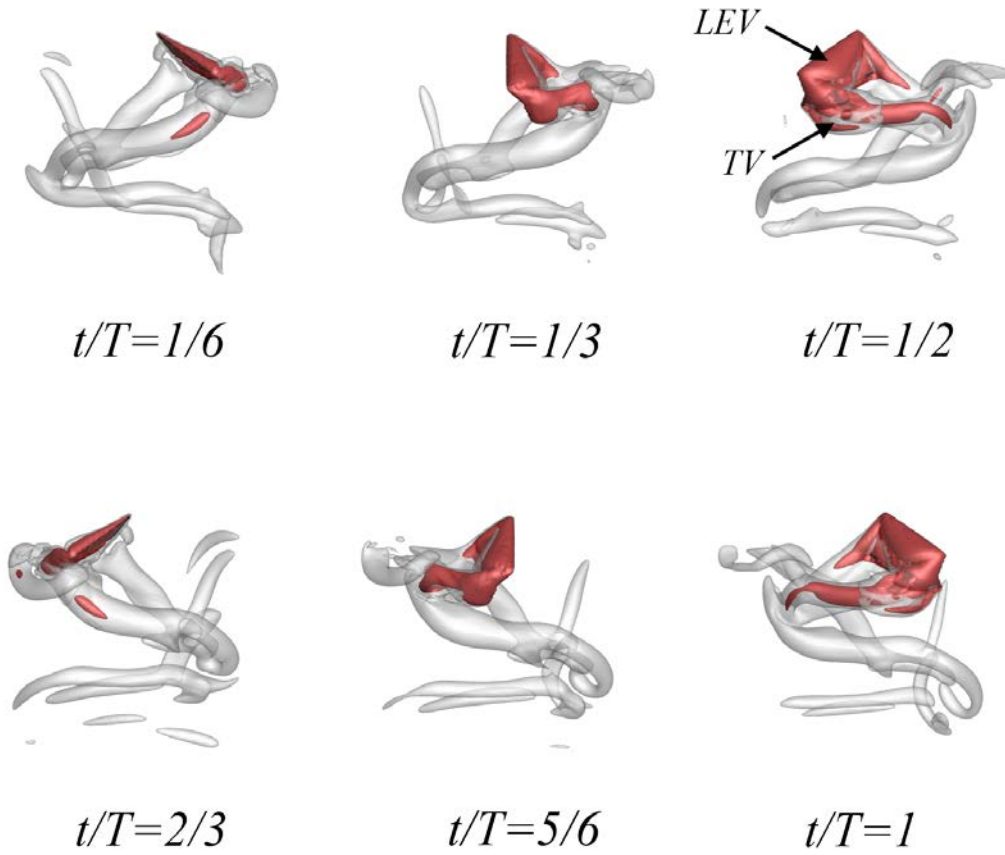
Figure 29. Vortical structure for plate with a right triangular trailing-edge shape (RTS) during the fourth flapping cycle.
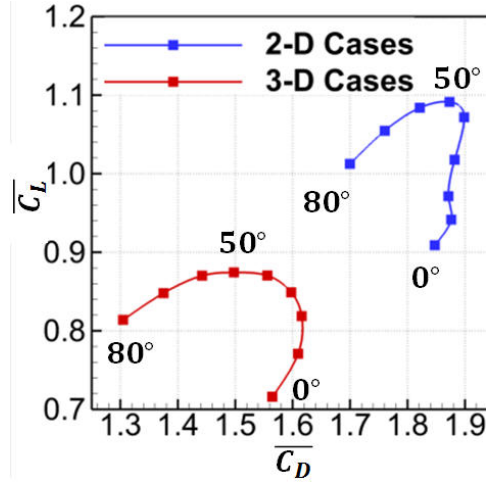
Figure 30. Polar plot of lift and drag coefficient for 2-D and 3-D cases at phase shift changing from 0 to 80 degrees.

Concluding Remarks:

The right triangle shape (RTS) trailing-edge can locally modify the vortex formation and delay the appearance of dynamic stall. Thus, it can enhance the unsteady lift production comparing to a fully rigid plate.

4.3 Understanding the flow physics of flapping/revolving plate

1) Hinge-connected hovering plate

In this work, deformable flapping wings are modeled as a hovering rigid membrane plate with prescribed leading edge kinematics. A torsional spring, whose stiffness is governed by a ratio of forced-to-natural frequency, is placed at the leading edge and driven sinusoidally with the deflection of the membrane determined by its interaction with the surrounding fluid. The effects of hinge stiffness and stroke amplitude are studied and aerodynamic performance is discussed therein. While hovering is the major impetus of this work, it is noted that this work could be adapted to study other flight modes, such as takeoff, cruising, and quick yaw turns, all of which are observed in nature and a desired attribute for most MAVs. The subsequent section discusses the related MAV design and parameters chosen for this study. To this end, a wide span of frequency ratios were selected to cover the spectrum from very loose hinges (1/3) to very stiff hinges (1/8). This range encapsulates many insect species and should be achievable in design as well. The choice of dimensionless stroke amplitude ranges from 0.5 to 6 and some specialty cases of 10 chords. This will cover many species from fruit flies and dragonflies all the way up to hummingbirds. The summary of parameter levels is shown in Table I.

Table I: Parameter choice for kinematics and hinge model

Parameter	Levels						
ω_f/ω_n	1/3	1/4	1/5	1/6	1/7	1/8	--
A_x/c	0.5	1	2	3	4	5	6

The Reynolds numbers in the simulations are all 188.4, which was chosen from within the feasible range for insect flights and also falls within the acceptable tolerance for DNS solvers such as this one. In our study, the mass ratio, given by (1) is 0.2.

$$M_R = \frac{\rho_s\, h}{\rho_f\, c} \tag{1}$$

The mass ratio of a cranefly and dragonfly is estimated to be 0.34 (Ishihara, Horie, & Denda, 2009) and 0.8 (Chen, Chen, & Chou, 2008) respectively. Thus, the wing in the current study is light and most analogous to a cranefly. The infinitely thin membrane assumption is made based on the case of a density ratio of 20, the ratio of thickness to chord length $\frac{h}{c} = 0.01$, which can be modeled as a membrane. Assuming the density ratio between solid and fluid increases and the wing material in air becomes denser, the thickness ratio further reduces, justifying the membrane assumption more easily.

The overall progression and wake formation of the flapping foil is discussed through subsequent z-component vorticity snapshots. Figure 31 shows one particular case of $\omega_f/\omega_n = 1/6$ undergoing kinematics with $A_x/c = 3$. This case was chosen specifically as a moderate range of motion with a relatively rigid hinge spring. The plots of vorticity are shown with contour levels from -5 to 5, where red contours show clockwise rotation and blue contours show counterclockwise rotation.
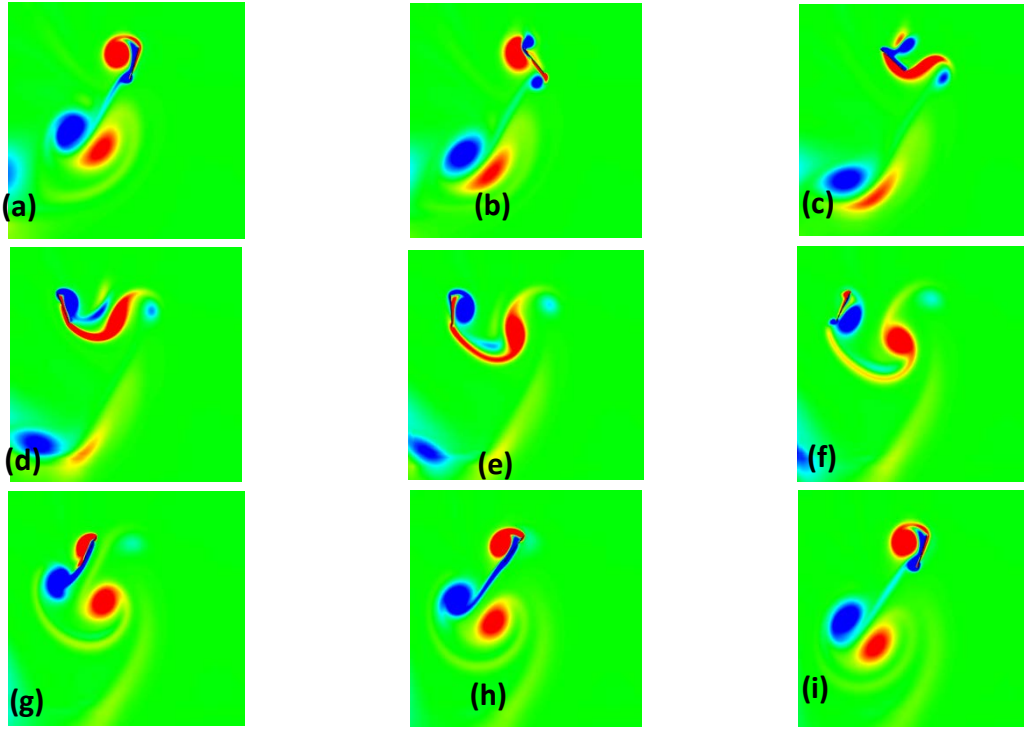
Figure 31. Vorticity contour snapshots for $A_x/c = 3$, $\omega_f/\omega_n = 1/6$. (a) t/T = 3.0, (b) t/T = 3.125, (c) t/T = 3.25, (d) t/T = 3.375, (e) t/T = 3.5, (f) t/T = 3.625, (g) t/T = 3.75, (h) t/T = 3.875, and (i) t/T = 4.0

The initial vorticity snapshot shown in Figure 31(a) is taken from the start of the fourth stroke cycle, at right extreme. A pair of counter rotating vortices that have been previously shed are located midway of the plates horizontal range of motion. The plate is initially inclined at a negative angle with respect to the motion of the leading edge. The torsional spring, which had been deflected in the upstroke of the previous cycle, has some stored energy, which is released at the point of stroke reversal, causing the plate to rotate faster than a freely pivoting hinge would allow. A leading edge vortex (LEV) from the previous stroke is fully developed and detached from the plate, while a trailing-edge vortex (TEV) is forming. As the stroke progresses and the plate begins to travel away from the right extreme, the previously formed LEV is reattached to the windward side of the plate, via wake capture, and a counter-rotating LEV is formed. The previously forming TEV separates from the plate and residual vorticity is convected from the leading to the trailing edge on the lee-side of the plate.

Now at the midpoint of downstroke, Figure 31(c), the plate is at its maximum velocity. The newly forming LEV is attached to the lee-side of the plate, which is responsible for the peak in lift production at midstroke. However, it is noted that the new LEV has a large diameter region where it appears to begin shedding. The reattached windward LEV is pushed to the trailing edge by the plate's motion and joined with the residual vorticity from the lee-side, now forming a new TEV. The stiffness of the spring along with the kinematics of the plate govern the deflection of the plate, for this particular choice of parameters, the plate remains a relatively high angle of attack (AOA) at midstroke, approximately 45°, causing the TEV to form with a larger diameter than those observed in plates whose mid-stroke AOA was diminished.

In Figure 31(d), as the stroke progresses, nearing reversal, the leading edge slows and the torsional spring begins to release energy causing the plate to rotate towards its equilibrium orientation (upright). This causes the LEV that appeared to be shedding at midstroke, to reattach to the lee-side. Upon stroke reversal, this LEV attachment will aid in wake capture, which will

38

promote a sudden increase in lift at the start of the upstroke. The plate rotation aids in separating the TEV, ultimately pushing it into the downwash. It is observed that as hinge stiffness increased, a larger amount of energy was stored in the torsional spring, causing the plate to rotate faster than weaker hinges (or freely pivoting plates) at stroke reversal, which, in turn, increased the downwash.
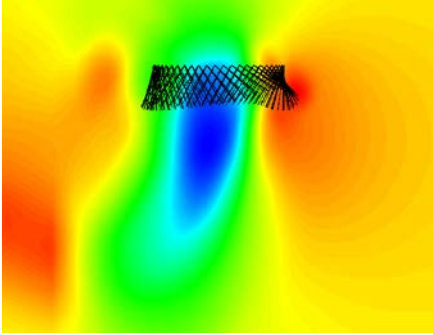
Figure 32. Cycle-averaged v-velocity contour for A_x/c = 3, ω_f/ω_n = 1/6

At stroke reversal, Figure 31e, the plate begins to move towards the previously formed LEV, supporting growth of a new TEV and the sudden change in direction and speed of the leading edge causes the formation of a new counter rotating LEV. As the plate moves to the midpoint of the upstroke, the LEV is attached to the lee-side of the plate once again. Comparing the LEV attachment in the up and down strokes reveals that the down stroke has better LEV attachment along the entire plate, causing the lift to have a higher peak value than in the upstroke.

The downwash of the plate is analyzed through a cycle averaged v-velocity contour, shown in Figure 32. The velocity field is averaged using data collected over 3 flapping periods. During these three strokes, 50 velocity field snapshots are collected for each period, and then averaged to create an average velocity field. It is important to analyze this field, as it provides information about the down wash and the overall energy in the flow. Over three periods, this particular case shows that a consistent and prolonged downwash (blue contours denote negative v-velocity) forms in the center of the stroke range. The downwash favors the initial motion direction, as this is where the first vortex is shed, causing the wake to bend in this general direction. It should be noted that the warmer (more red) colors denote a positive v-velocity (upwards). This phenomenon tends to occur outside the stroke reversal pointes, showing a clear downwash channel within the confines of the plate's motion. It should be noted that this selected case was a high-lift generating case with good overall performance metrics.

Instantaneous lift and drag coefficients are shown in Figure 33 for a sweep of various stroke amplitudes for a given frequency ratio. The drag coefficient peaks vary inversely with stroke amplitude; as the stroke range increases, the peaks (and averages) of drag decrease. An extreme range of motion (A_x/c = 10) is shown to illustrate the overall trend of the drag coefficient. As the stroke amplitude case increases maximally, the plate tends to incline to very low angles of attack, and the drag profiles within this long translation of the plate favor trends of static, fixed aircraft behaviors. However, as the stroke reverses, vortices are shed, and force oscillates while the plate changes direction. This is to be expected with flapping airfoils.
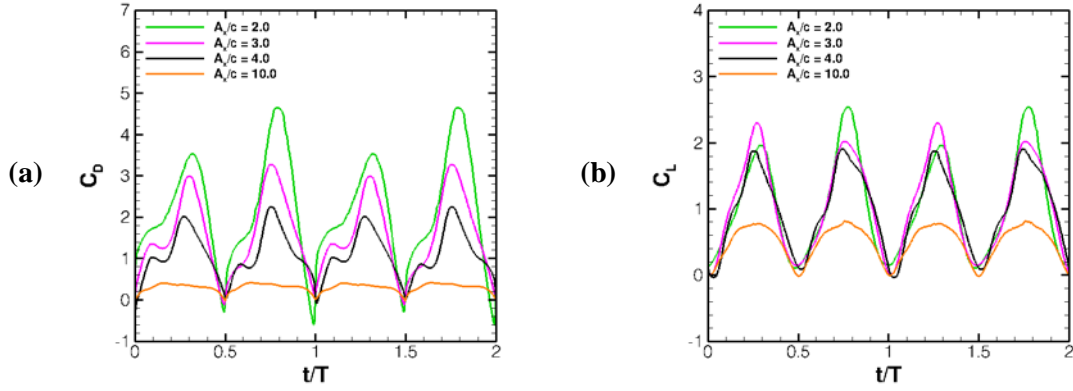
Figure 33. Stroke amplitude effects on instantaneous C_D and C_L for $\omega_f/\omega_n = 1/6$

Figure 34 shows the effects of frequency ratio for a fixed kinematic profile on instantaneous lift and drag coefficients. It should be noted that more rigid (stronger torsional springs) hinges have smaller frequency ratios than the loose hinges. It is shown that trends remain consistent across all frequency ratios for drag coefficient. However, as stiffness reduces, the peak drag coefficients also reduced. This was expected, as the less rigid hinge deflects much easier, resulting in a lower angle of attack.
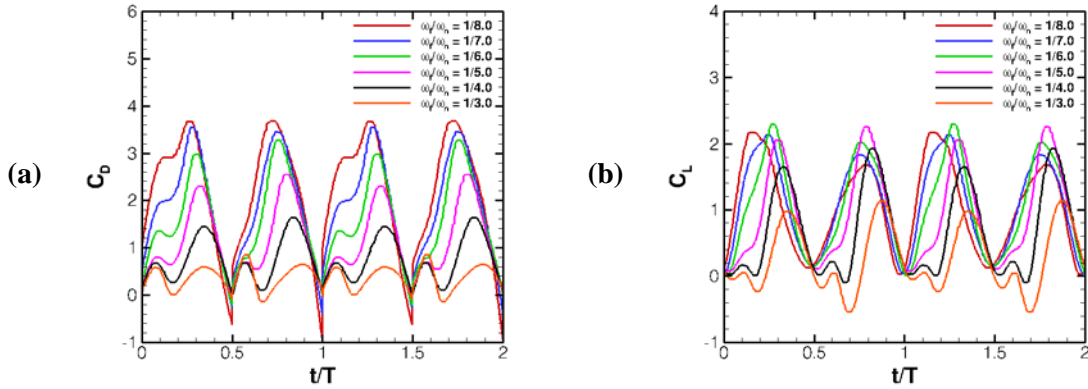
Figure 34. Frequency ratio effects on instantaneous C_D and C_L for $A_x/c = 3$

Concluding Remarks:

Deformable flapping wings are modeled as a hovering rigid membrane plate with prescribed leading edge kinematics. A torsional spring, whose stiffness is governed by a ratio of forced-to-natural frequency, is placed at the leading edge and driven sinusoidally with the deflection of the membrane determined by its interaction with the surrounding fluid. A region of kinematic profile is excluded from the design space due to complications with performance. This range includes all $A_x/c < 2$. The reason for such performance degradation is linked to the range of motion. For small amplitudes, the plate never has enough distance to travel to allow the plate to rotate through and give a positive angle of attack (in reference to the leading edge motion), especially for loose hinges. This is why loose (or free-to-pivot) hinges over small stroke amplitudes don't

generate a positive or reasonable amount of lift. The stiff hinges over small amplitudes ($A_x/c < 2$) outperform the loose hinges because the spring allows the transfer of potential energy, in the spring, to kinetic energy, in the plate's rotation, at stroke reversal, allowing the plate to accrue a positive (and more beneficial) angle of attack before a loose (or free-to-pivot) hinge can do so under the same kinematics. This release of energy is essential in achieving benefits from wake capture as well as properly generating downwash.

It was observed that performance benefits were found for an increase in stroke amplitude via a reduction in drag, increase in lift, and decrease in RMS force oscillations. Because of this, lift-to-drag ratio, aerodynamic input power and efficiency all profited. For each stroke amplitude, stiffness can be tailored to improve flight performance. However, a bifurcation point at ω_f/ω_n = ¼ suggests that the ideal spring stiffness belongs at or near this frequency ratio.

To suggest a MAV concept design based on the results of this study, it would be beneficial to have the largest stroke amplitude possible within the design limitations. It is also suggested that the ideal frequency ratio governing hinge stiffness should be chosen as ω_f/ω_n = ¼. Another interesting thing can be noted about this choice of parameters. Reviewing the kinematics and known frequency ratios of dragonfly wings, this optimal MAV design parameter choice coincides with the operating range of dragonflies. This suggests that one of nature's best flyers operates at a parameter range known to have an optimum flight performance discovered in this study, further supporting the idea that MAVs should be bio-inspired designs.

2) Hovering hinge-connected flapping plate with passive deflection

It is undoubtedly important to understand the aerodynamics of flexible wings to improve the Micro Aerial Vehicle design. The flexibility mechanism and its effects on aerodynamic performance are not fully understood yet and still attract a lot of attention. In this sub-section, two types of hinged plate in hovering are studied, as shown in Figure 35. The first type is a one-link plate with free-to-pivot hinge at the leading edge, which is constrained moving horizontally according to a prescribed function given by Eq. (1) :

$$x(t) = \frac{A_x}{2}\cos(2\pi ft), \quad y(t) = 0, \tag{1}$$

in which the spatial coordinates in Cartesian system are denoted by x and y respectively, f is flapping frequency and t is time. The deflection angle θ_1 is unknown and is determined from interaction between fluid and body. The effects of stroke amplitude on the aerodynamic performance of one-link plate is studied. As the stroke amplitude varies, the flapping frequency is adjusted accordingly to keep the Reynolds number invariant.

The second type is a two-link plate, in which the translation of the leading edge is given by Eq.(1), and the deflection angle θ_2 of the upper link is prescribed by Eq. (2):

$$\theta_2(t) = A_\theta \sin(2\pi ft) \tag{2}$$

The lower link is connected to the upper link by a free-to-pivot hinge, and is subjected to the fluid-body interaction and passive deflection. The prescribed translation and rotation function have a phase difference of $\pi/2$ internally by the given cosine and sine functions respectively. In the two-link plate, the hinge location is changed from the leading edge to the three-quarter chord (near the trailing edge), and its effects on aerodynamic performance and power consumption are investigated. A ±45° inclination limiter is applied to confine the maximum passive deflection angle, so that a comparison on aerodynamic performance can be made with that obtained from full-body prescribed motion.

41
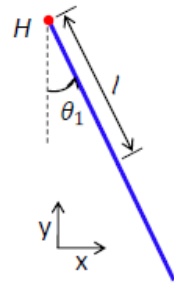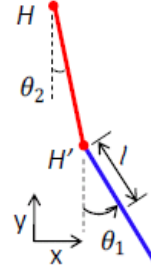
(a) One-link plate (b) Two-link plate

Figure 35. Plate with hinge(s). For the rigid (one-link) plate, the prescribed motion is given at the leading edge (H); for the two-link plate, the prescribed motion is given on the upper link (H H′).

a) $t/T = 0$ b) $t/T = 0.125$ c) $t/T = 0.25$ d) $t/T = 0.375$

e) $t/T = 0.5$ f) $t/T = 0.625$ g) $t/T = 0.75$ f) $t/T = 0.875$
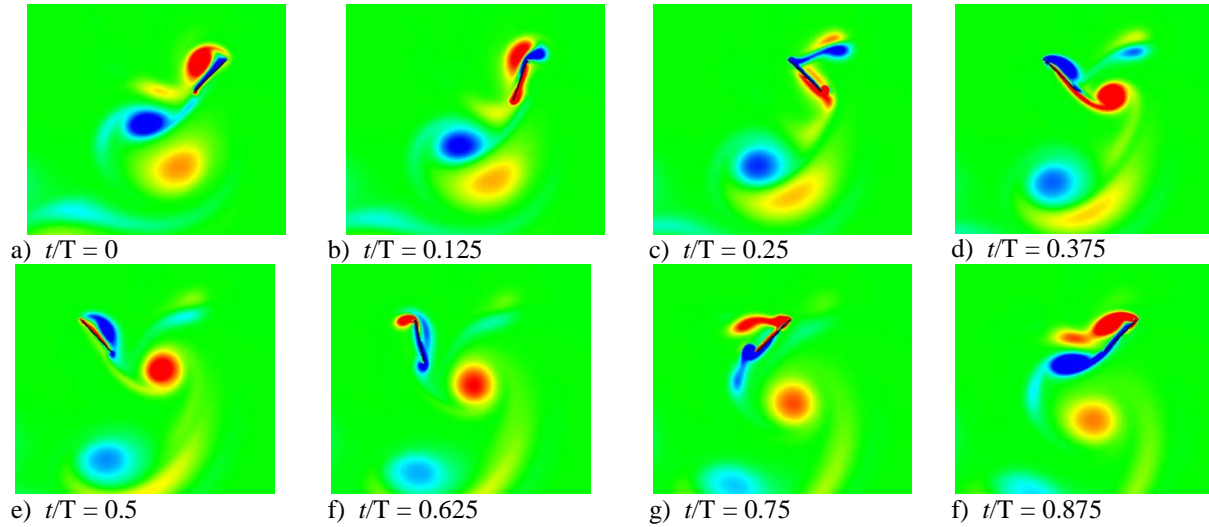
Figure 36. Vorticity snapshot for leading edge hinged plate, with $A_x/c = 3$.

In one-link plate, the leading edge (hinge) moves horizontally according to prescribed motion Eq.(1), with various stroke-to-chord ratio or Strouhal number ($\frac{c}{\pi A_x}$). Figure 36 has shown the snapshot of vortex development over one cycle after stable flapping is obtained, for the case of stroke-to-chord ratio 3. At $t/T = 0$, the leading edge of the plate is at the right extremum. The trailing edge of the plate, however, inclines at a certain angle, due to delayed rotation. Similar phenomena is shown in Granlund et al. [13]. At $t/T = 0.125$, the leading edge of the plate moves to left horizontally, a pair of vortices start to shed from the leading edge, with an upward direction component. Thus, a negative lift can be generated at this moment. The trailing edge moves downwards, producing a trailing edge vortex (TEV) in the counter-clockwise direction. At $t/T = 0.25$, the inclination angle has reached its limiter, and is constrained at 45°. A pair of leading edge vortices (LEV) has been shed, and new vortices start to develop due to the translation at the leading edge and the trailing edge respectively. At $t/T = 0.375$, a strong LEV is obtained and attached to the lee side of plate. A fully developed TEV has been shed and is connected to the trailing edge of the plate by a stretched vortex sheet. At $t/T = 0.5$, the lead edge of the plate reaches the left extreme. The LEV has been shed and stays above the plate,

42

indicating a low pressure region above the plate. A similar vortex pattern is obtained at the second half stroke cycle.

Table II has listed the averaged force coefficients, lift-to-drag, lift-to-power ratios generated by plates flapping at different stroke-to-chord ratios. Apparently, the lift-to-drag coefficient deteriorates as the stroke-to-chord ratio reduces in the range we have studied. Figure 37 shows the variation trends of $\overline{C_L}/\overline{C_D}$ and $\overline{C_L}/\overline{C_{PW}}$ as stroke range increases. It can be seen that both lift-to-drag ratio and lift-to-power ratio rise quickly as the stroke-to-chord increases from 2 to 4. As A_x/c is greater than 4, $\overline{C_L}/\overline{C_D}$ and $\overline{C_L}/\overline{C_{PW}}$ rise slowly and will level off eventually. The improved efficiency factor $\overline{C_L}/\overline{C_{PW}}$ indicates more input power is used to generate the lift at longer strokes.

Table II: Aerodynamic coefficients at various stroke-to-chord ratio

$\dfrac{A_x}{c}$	$\overline{C_L}$	$\overline{C_D}$	$\overline{C_L}/\overline{C_D}$	$\overline{C_L}/\overline{C_{PW}}$
6	0.684	1.348	0.507	0.606
5	0.625	1.275	0.490	0.596
4	0.547	1.260	0.434	0.539
3	0.453	1.207	0.375	0.472
2	0.088	1.319	0.067	0.082
1	-0.541	1.249	-0.433	-0.493
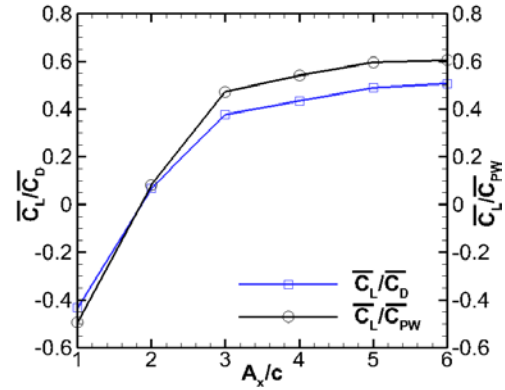
Figure 37. Lift-to-drag and Lift-to-power ratios versus stroke amplitude

We move the hinge location from the leading edge to the trailing edge, and investigate the aerodynamic performance as the hinge location varies. The translation and rotation of the upper link are prescribed by Eqs. (1) and (2), in which $A_x = 3.0$ and $A_\theta = \pi/4$. Thus $A_x/c = 3$, which is a typical stroke-to-chord ratio. Figure 38 shows the vorticity snapshot of a hovering plate with a hinge at one-quarter (denoted as 1QH) chord over one cycle, after the stable flapping has obtained. At $t/T = 0$, the upper link is vertical at this instant. Due to the delayed rotation, the lower link inclines with respect to the upper link. A larger LEV is developed from the previous stroke, compared with the LEV shown in Figure 36(a). In other words, a prescribed small portion of upper link can improve the development of LEV. At $t/T = 0.125$, the upper link and lower link form a camber, which facilitates a better capture of LEV. Part of the captured LEV then will flow down along the lower link. At the same time, a TEV starts to develop at the lee side of lower link. At $t/T = 0.25$, the inclination limiter has been reached. The part of captured LEV has moved down to the trailing edge and merged with TEV generated by the rotation of lower link. At the leading edge, a pair of vortices has been shed, and a new LEV is generated by motion of the upper link. At $t/T = 0.375$, a stronger LEV is developed over the lee surface of the plate, compared with the LEV in Figure 36(d). A vortex sheet emanates from the trailing edge, eventually rolling up, and combines with the shed TEV. At $t/T = 0.5$, the upper link returns to vertical orientation, with a fully developed LEV at lee side. Again, the size is larger than its counterpart in Figure 36(e).

43

a) $t/T = 0$ b) $t/T = 0.125$ c) $t/T = 0.25$ d) $t/T = 0.375$

e) $t/T = 0.5$ f) $t/T = 0.625$ g) $t/T = 0.75$ h) $t/T = 0.875$
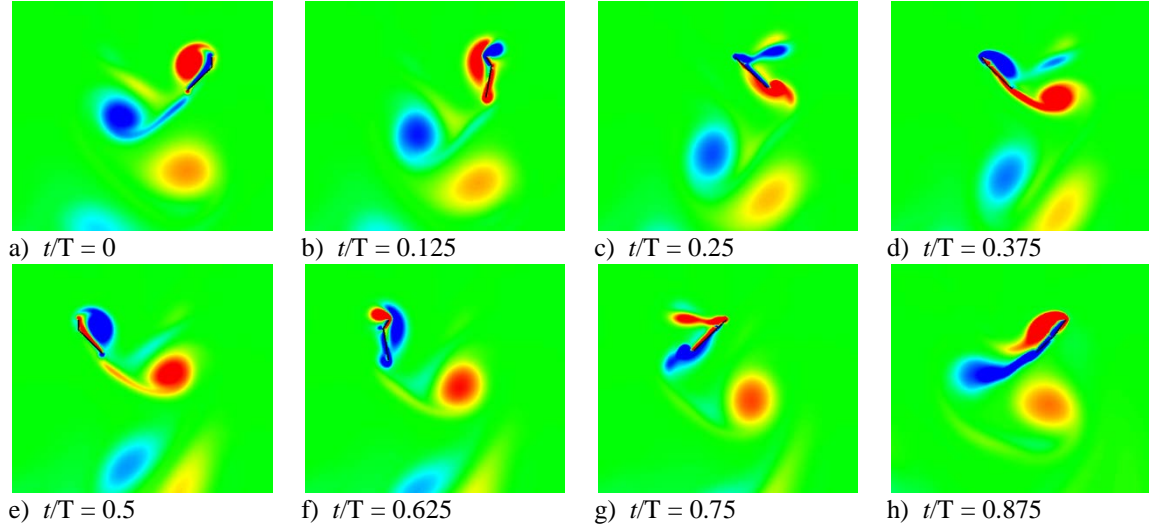
Figure 38.   Vorticity snapshot of plate with one-quarter hinge (1QH), $A_x/c = 3$.

Figure 39 shows the variation of averaged lift-to-drag, lift-to-power ratios as the hinge location moves away from the leading edge for three various stroke-to-chord ratios. Hinge location 0 and 1 are corresponding to cases of LH and Prsb respectively. First, for all the three cases, $\overline{C_L}/\overline{C_D}$ and $\overline{C_L}/\overline{C_{PW}}$ increase as the hinge moves down along the chord. Depending on stroke amplitude, the best performance can be obtained when the hinge is at a location near three-quarter or mid-chord. Compared with rigid body under prescribed motion, higher lift-to-drag ratio can be achieved with less power input in the case of 3QH. Second, the effectiveness of improving performance by varying hinge location is affected by the stroke amplitude. At $A_x/c = 2$, rising of $\overline{C_L}/\overline{C_D}$ or $\overline{C_L}/\overline{C_{PW}}$ is dramatic; at $A_x/c = 5$, the improvement on those ratios is mild. Third, the plate with flexibility does not guarantee the better aerodynamic performance compared with the fully prescribed rigid body. For example, performance in cases of 1QH, MH with $A_x/c = 2$, 1QH with $A_x/c = 3$ is inferior to that of rigid body. Thus, aerodynamic performance can be augmented by plate flexibility only when the appropriate hinge location is selected.

a) $A_x/c = 2$ b) $A_x/c = 3$ c) $A_x/c = 5$
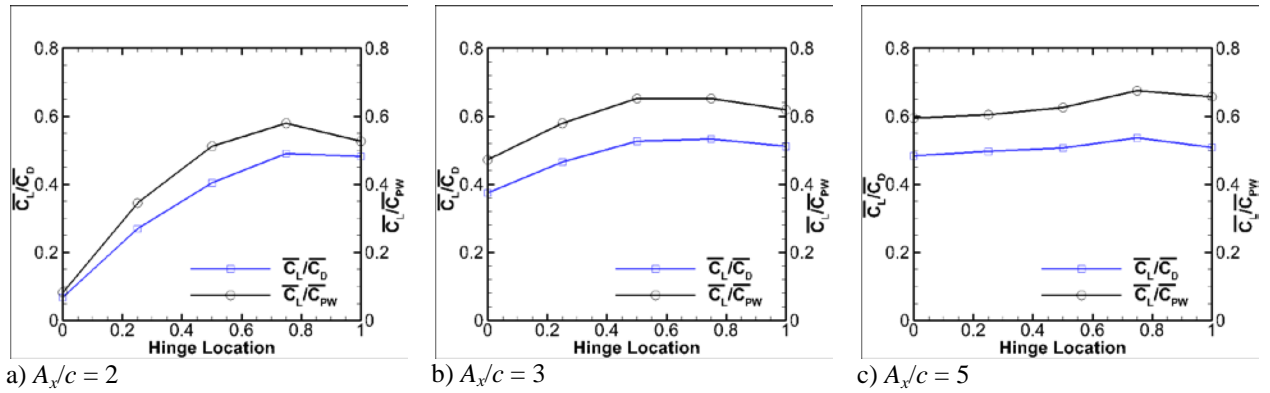
Figure 39. Variation of Lift-to-drag and Lift-to-power ratios as hinge location changes.

Concluding remarks:

44

Hovering hinged plate is numerically simulated as a fluid-body interaction problem to study the effects of passive deflection. A ±45° inclination limiter has been used to constrain the maximum incidence angle of hinged plate, whose orientation is determined by its interaction with surrounding fluids. Two types of cases have been investigated. The study of stroke-to-chord ratio effect (equivalent to Strouhal number effect in the case of hovering plate) on aerodynamic performance of a rigid body with passive rotation is conducted first. As the stroke amplitude reduces, the averaged lift-to-drag ratio decreases, suggesting worse aerodynamic performances. When the plate flaps with very small stroke amplitude, the averaged lift can be negative, indicating an inverted hovering motion. The plate with chord-wise flexibility is modeled by a two-link mechanism connected by a hinge, which is varied along the chord. The aerodynamic performance gets improved in terms of increased lift-to-drag ratio as the hinge location moves down from the leading edge. Compared with the rigid body under fully prescribed motion, higher lift-to-drag ratio can be obtained with less input power by the plate with hinge at three-quarter chord (near the trailing edge). The effectiveness of improving aerodynamic performance by varying the hinge location is limited to small or medium stroke amplitude (Ax/c < 3 in our study). Also, the chord-wise flexibility does not guarantee the increased lift-to-drag ratio, or reduced power consumption, with respect to those from fully prescribed rigid plate. The benefits of chord-wise flexibility can only obtained when the hinge location is carefully selected. It is a tradeoff between the lift sacrifice and drag reduction, which are two effects simultaneously brought in the game by the flexibility.

3) Flow structures and aerodynamic performance in low aspect ratio revolving plates at low Reynolds number

Understanding of vortex formation and aerodynamic loading is important for studying rotor wake and rotary-winged micro air vehicles. In this work, direct numerical simulation (DNS) is used to study three-dimensional flow structure and aerodynamic performance of low aspect ratio revolving plates in Reynolds number 500 flows. These plates are modeled as rectangular plates with zero thickness at a fixed 30° angle of attack. The span varies from 1 to 4 times of the chord length. A total rotation of five cycles ($\phi=10\pi$ radians) and a matched tip Reynolds number of 500 are used in all cases. In general, the flow initially consists of a connected and coherent leading-edge vortex (LEV), tip vortex (TV), and trailing-edge vortex (TEV) loop; the span-wise flow is widely present over the plate and the wake region. After impulsive start, both forces and power coefficients are reduced by as much as 30 percent of the maximum value at the end of first cycle. When plate aspect ratio increases, hairpin-like vortical structures are formed at the wing tip and further affect the stability of the wake structure due to the wing-wake and wake-wake interaction. Depending on the aspect ratio, the force and power coefficients take different amount of period to reach to a stationary stage.

Figure 40 shows the vortex structures generated by revolving plate of AR=1, 2 and 4 in quiescent flow. Plates rotate with respect to the positive y-axis. Iso-surface of Q=1.0 are used. Generally, a dipole structure starts to form after revolving plate rotates 90°. The two vortex structures shedding from LEV and TV are mixed together with different rotation velocity. This phenomenon is more obvious for *AR*=4 case. When plate aspect-ratio increases, hairpin-like vortical structures are formed at the wing tip and further affect the stability of the wake structure
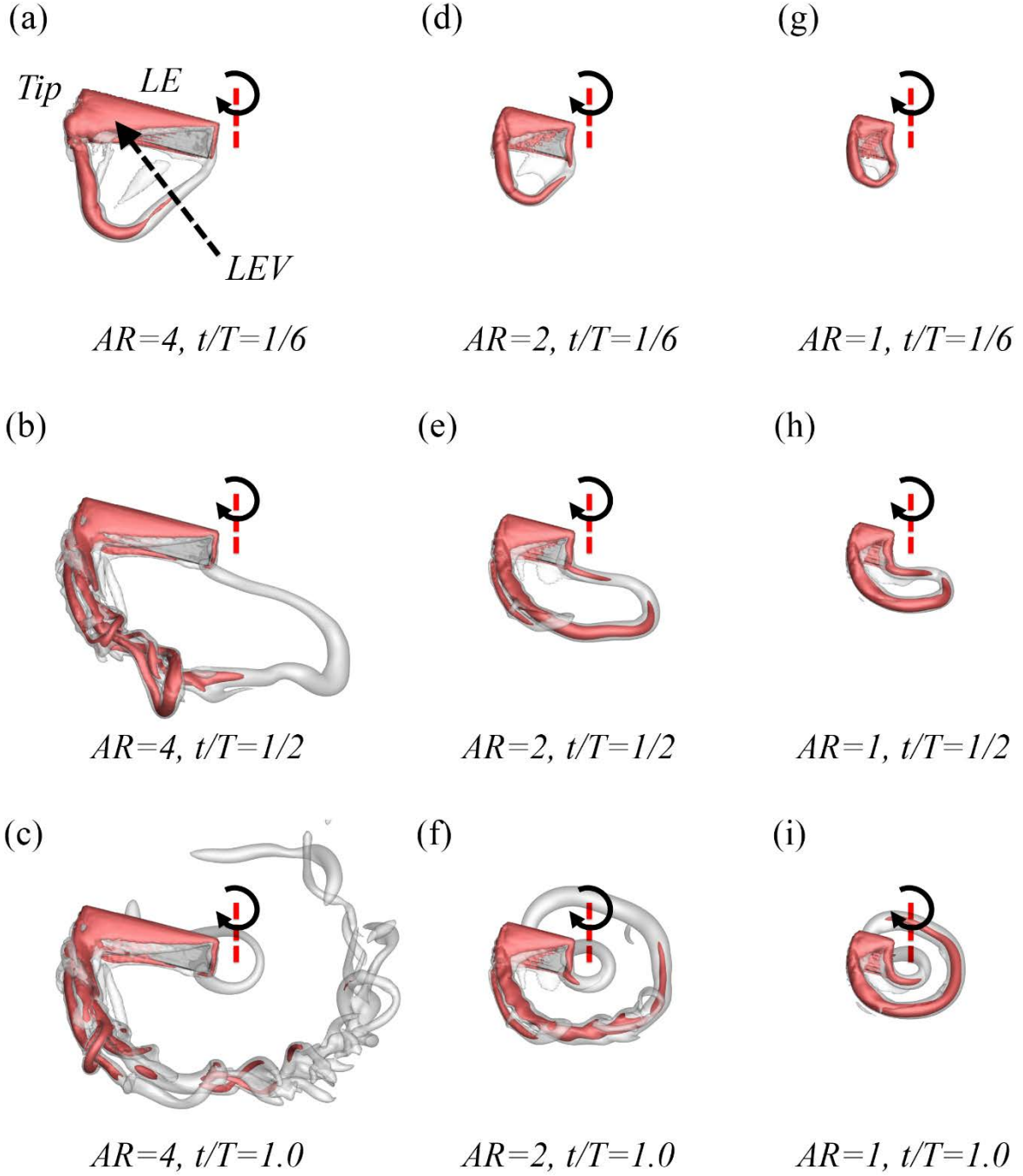
Figure 40. Comparison of vortex structures of the first revolving cycle for AR=4 (a-c), AR=2 (d-f), and AR=1 (g-i) for different ϕ. The three-dimensional flow structures are shown for different rotational angles through iso-surfaces. Two surfaces are shown to highlight the inner core (Q=1.0) and outer shell (Q=3.0) of the vortex structure.

due to the wake-wake interaction. After a whole $180°$ rotation, a horse shoe like vortex structure is formed. At far flow field, because of the rotary motion, vortex shedding from current cycle can interact with the previous wake structure. For a matched tip Reynolds number, higher *AR* plate shows much stronger interaction between the wake created in the current rotation cycle and the previous one. The unsteady tip vortex formation is more obvious for *AR*=4 case.

Figure 41 gives the time courses comparison of lift coefficient (C_L) and drag coefficient (C_D) and of plates with AR =1, 2 and 4 in a complete five rotational cycles ($\phi=10\pi$) under a fixed 30° angle of attach and Re_{tip} =500. The force and power coefficients are all respect to its local coordinates. During the rotational motion, the instantaneous aerodynamic performance generated on the wing for each aspect ratio case shares the similar decreasing and increasing tendency (during t/T=1.0 to 2.5) and gradually reach to a constant value once the flow reaches a nearly stationary state. At the first rotational cycle, both aerodynamic force and power coefficients are shown a larger value because of the impulsive start. The similar observation also presented in [14] by comparing the revolving motion and flapping motion for a pair of hawkmoth wing model.
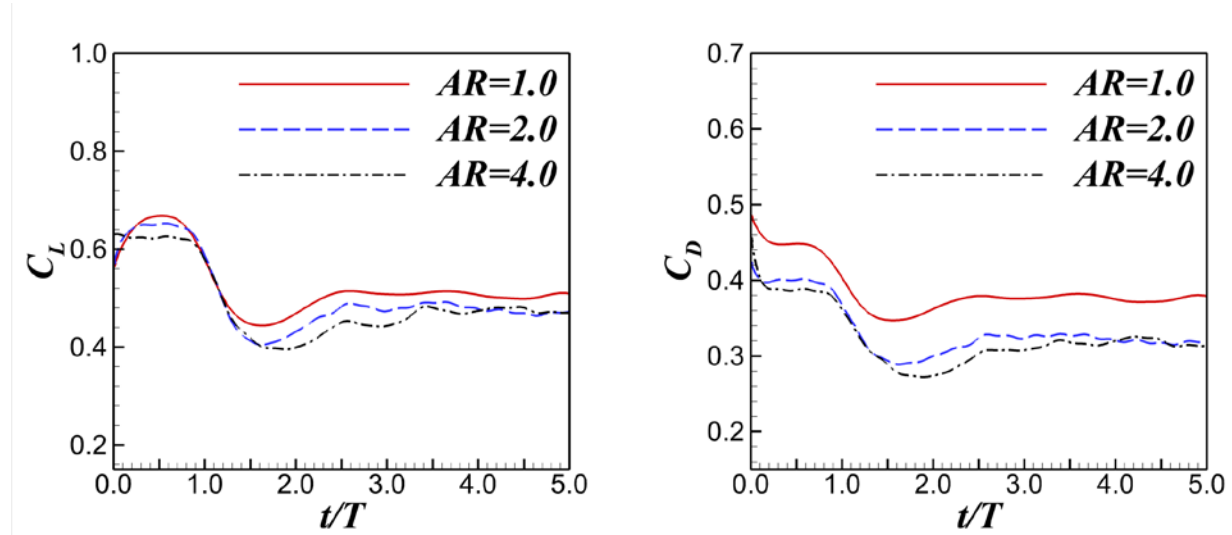
Figure 41. Comparison of instantaneous lift and drag coefficient for the case with different aspect ratio (AR).

Concluding Remarks:

After the initial start-up, both lift and drag coefficients are reduced by as much as 30 percent of the maximum value at the end of first cycle. In addition, for a fixed tip Reynolds number, the increasing of aspect ratio will delay the flow reach to a steady stage. Depending on the aspect ratio, the force coefficients take different amount of period to reach constant values. Furthermore, wing-wake and wake-wake interactions are much stronger for large aspect ratio case. This is mainly because of the extra span-wise flow generated cannot be feed into the main vortex ring via the shear layer. This extra shed vorticity further form a hairpin-like vertical structures and interact with each other, and become the main source of instability. In sum, for a fixed tip Reynolds number, the larger aspect ratio cases present more unstable vortex formation. For a fixed tip Reynolds number, whether there exists an optimal AR-to-ω ratio to make the span-wise flow continually feed into the main vortex loop and thus improve the aerodynamic performance still need further investigation.

4) Symmetry of proper orthogonal decomposition modes of a low-aspect-ratio flapping plate

In this work, the symmetry property and corresponding virtual force contribution of the proper orthogonal decomposition (POD) modes are numerically investigated for the flows generated by a low-aspect-ratio plate undergoing a pitching-plunging motion. It is found that the flow and its POD modes have the same reflectional symmetry about the spanwise central plane. However, about the crossflow central plane, a half-period symmetry of the flow results in a symmetry change every two POD modes, which corresponds to odd or even multiples of the vortex shedding frequency. Based on a wake survey method, the POD modes are classified into two categories of thrust and lift producing. Furthermore, the thrust and lift producing modes are shown to have distinct symmetry properties, which can be used to identify the correlation between the wake structure and the hydrodynamic force generation.

In Figure 42, flow visualizations of three-dimensional structures are mainly based on iso-surfaces of *Q-criterion* [29], which are colored by intensity of certain vorticity components for indicating the direction of vortices. The vortex structures at time $t/T=0$ and $1/2$ are two series of vortex rings which convect vertically in opposite directions while traveling downstream. The upward vortex rings are counterclockwise (CCW) and those downward are clockwise (CW) when viewed from the top. At time $t/T=0$, the plate is at the lowest position and starting to move upward. A downward vortex ring has shed out its trailing edge vortex near the plate. A complete vortex ring will form after the leading vortex is shed at $t/T=1/4$. Then another vortex structure begins to form at the leading edge of the plate. Because of the upward motion of the plate, it will form an upward traveling ring structure finally. The profile of vortex structures has a small aspect ratio when it attaches to the plate. However, after shedding out, it is quickly elongated in the Z-direction and gradually rounds off.
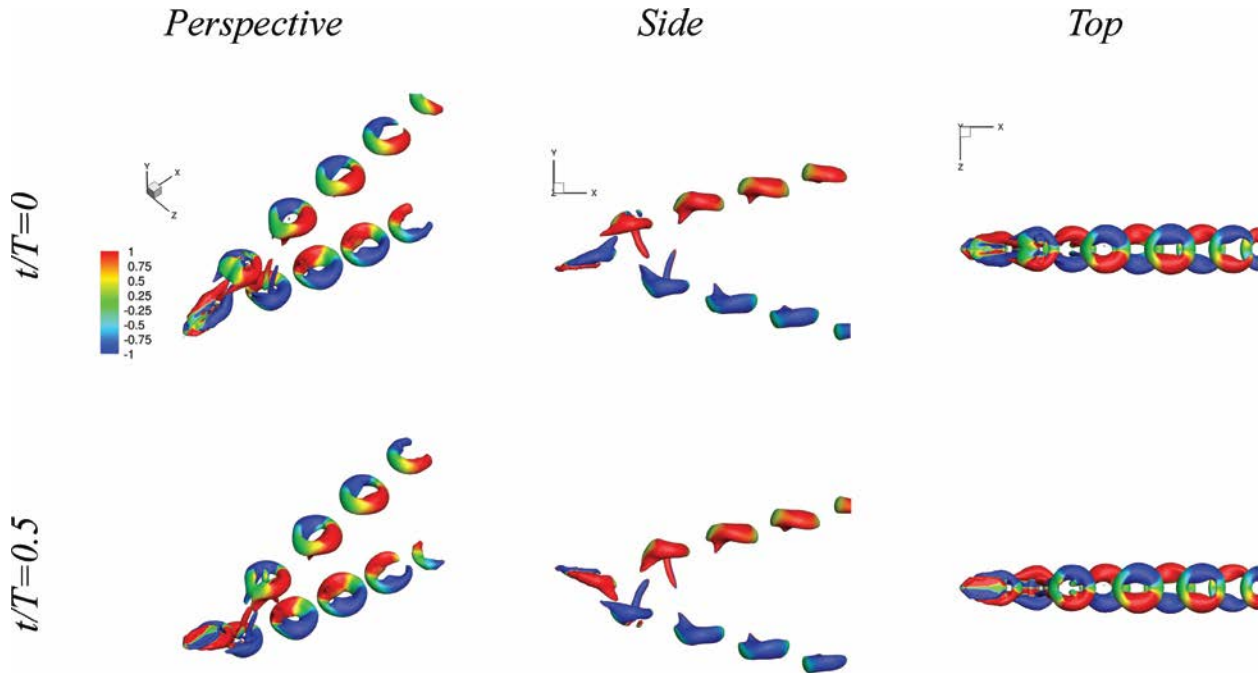

Figure 42. The vortex formation viewed from different angles, colored by the X-direction vorticity ω_x. $Q=0.25$.

The major structures in the mean flow wake, which is obtained by averaging the data ensemble, are four straight vortex tubes that are spatially antisymmetric about the *XY-* and *XZ-*

plane, as indicated by the averaged X-direction vorticity $\bar{\omega}_x$ (Figure 43 (a)). Because the vorticity components in Y- and Z-directions have much smaller magnitudes, these vortex tubes are considered to represent the transport of X-direction vorticity. This is different from two-dimensional flows, in which only the Z-direction vorticity is nontrivial.

We use POD mode to decompose the flow filed. Contribution of individual eigenvalues to the total fluctuating kinetic energy with respect to the mean flow wake can be expressed as normalized eigenvalues in a form of $\lambda_i \Big/ \sum_{k=1}^{N_m} \lambda_k$. Captured energy by the first i modes can be represented by $\sum_{k=1}^{i} \lambda_k \Big/ \sum_{k=1}^{N_m} \lambda_k$. The values of the first six modes are listed in Table III. Curves of normalized eigenvalues and captured energy with respect to the number of POD modes are shown in Figure 43 (b). Here, every two eigenvalues form a pair with approximate values for the first several modes. The first two modes contain about 41% and 35% of the total fluctuating kinetic energy, respectively. The third and fourth modes account for lower energy at about 7%. The cumulative energy up to the 6th mode is over 96%. This means that the first six modes capture a majority of large flow features including the vortices near the flapping wing and the vortices in the far wake zone. This is in consistent with previous studies on flapping wings.

The topology contours of POD modes 1 to 6 are shown in Figure 44. The first mode contains a doughnut-shaped vortex structure followed by two rows of chain vortices that extend downstream with an inclination angle to the *XZ-plane*. The vortex rings on the chain vortices switch rotational direction between CW and CCW when viewed from the top. The topology pattern of the mode 2 is similar to that of the mode 1, with one quarter wavelength shift of each vortex ring along the vortex chains. This is shown by the color change of Ψ_x in the side view.

The topology structures of the modes 3 and 4 are bifurcated vortex formations, which consist of irregular vortex structures instead of round rings. The widths of the chains are approximately the same in the Z-direction. The $\pi/2$ phase difference between the modes 3 and 4 is indicated by the color switching of Ψ_y. The modes 5 and 6 have the similar topology structures as that of the modes 3 and 4. Here, the phase shifting is indicated by the color change of Ψ_x. It is also shown that the fluctuating kinetic energy dissipates rapidly in the downstream for the higher modes.

Table III: Contribution of the first six eigenvalues to the total fluctuating kinetic energy

Mode	Contribution(%)	Accumulation(%)
1	41.4	41.4
2	34.7	76.1
3	8.3	84.4
4	7.8	92.2
5	2.3	94.5
6	2.0	96.5

Special symmetry patterns are distinguishable in the topology of the POD modes, as listed in Table IV. The terms "*S*" and "*A*" denote symmetric and antisymmetric, respectively. A similar velocity symmetry table can be made by simply switching "*S*" and "*A*" in Table IV. Note that

each pair of the POD modes that have close eigenvalues has the same symmetry property. According to symmetry, the POD modes can be categorized into two sets, G_1 and G_{-1}, where $G_1=\{x:$ mean or modes 3, 4, 7, 8, ..., 43, 44, 47, 48$\}$ and $G_{-1}=\{x:$ modes 1, 2, 5, 6, ..., 41, 42, 45, 46$\}$. It is worth to point out that the symmetry property of the POD modes is independent of the selection of domain size for computing the POD modes.
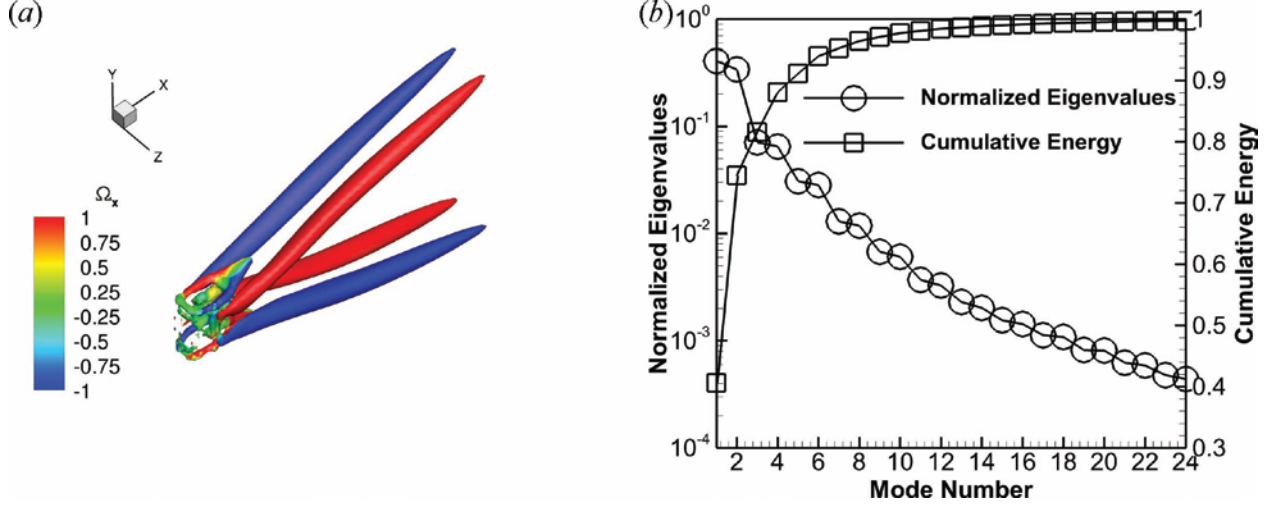

Figure 43. (a) Iso-surface of the *Q-criterion* of mean vorticity colored by the X-direction vorticity $\overline{\omega}_x$. $Q=0.25$; (b) Normalized eigenvalues (circle) and captured energy by the first i modes (square) versus mode number $i=1, 2… 24$.

Table IV: Vorticity symmetry of the mean flow and POD modes

Vorticity	Mean			Mode 1, 2			Mode 3, 4			Mode 5, 6		
	$\overline{\omega}_x$	$\overline{\omega}_y$	$\overline{\omega}_z$	Ψ_x	Ψ_y	Ψ_z	Ψ_x	Ψ_y	Ψ_z	Ψ_x	Ψ_y	Ψ_z
XZ-plane	A	S	A	S	A	S	A	S	A	S	A	S

 We apply the POD-FSM to the flow to calculate the effect of symmetry of POD modes in terms of virtual forces. Adding all forces of POD modes can calculate the total force acting on the plate, as shown in Figure 45. Force reconstruction with 48 modes converges to the results of the impulse equation[17]. The time-average and RMS thrust coefficients are 0.270 and 0.404, respectively. The time-average and RMS lift coefficients are 0.048 and 2.019, respectively. These values show a slight deviation from the DNS results. The role of high order POD modes is examined by using 24 and 48 modes respectively. It indicates that the forces computed from 24 and 48 models are highly similar to those calculated from the impulse equation. Few larger deviations can be observed near *t/T*=0. It implies that the interaction between low-energy modes and other modes can hardly affect the total force acting on a pitching-plunging plate in low Reynolds number flows.

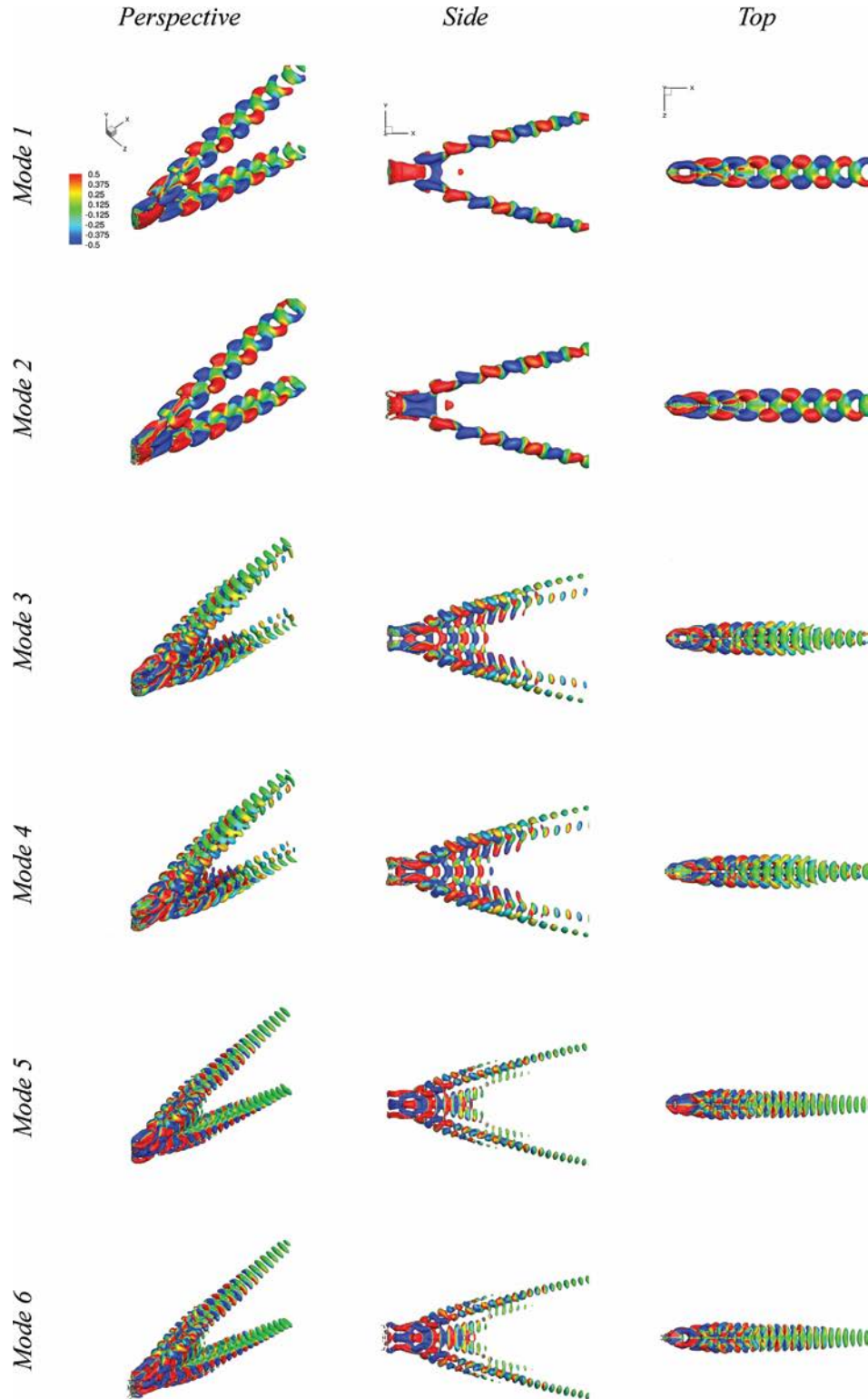**Figure 44.** Iso-surfaces of *Q-criterion* of POD modes from 1 to 6. The iso-surfaces of the modes 1, 2, 5 and 6 are colored by the X-direction vorticity Ψ_x. The modes 3 and 4 are colored by the Y-direction vorticity Ψ_y. $Q=0.0625$.

51

The power spectrum of the force acting on the plate shows that the lift and thrust consist of odd and even harmonics, respectively. According to the symmetry property of POD modes, modes in G_1 are found only producing thrust, and modes in G_{-1} are only responsible of lift production. Using this criterion, the original flow can also be decomposed into thrust and lift producing flows. This approach is expected to be applicable to other mode decomposition methods, such as balanced POD [30] and dynamic mode decomposition [31], which are capable of extracting symmetric wake structures.
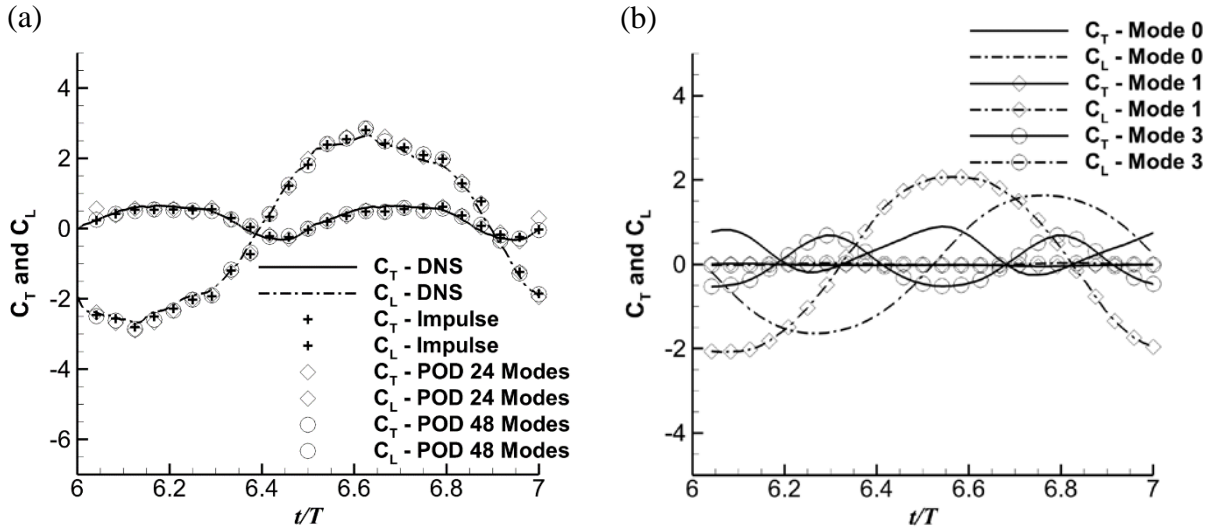
Figure 45. Thrust and lift coefficients from DNS, the impulse equation and the POD-FSM with 24 or 48 POD modes. (b) Virtual thrust and lift coefficients of the mean flow, the POD modes 1 and 3.

Concluding Remarks:

By conducting a POD analysis of the original flow, we found that the first six modes contain 96% fluctuating kinetic energy of the flow. All the POD modes have the same symmetry property about the Z central plane as the original flow. About the Y central plane, the modes 1 and 2 are reflected and reversed but the modes 3 and 4 are only reflected.

52

4. References

[1] M.H. Dickinson, F.O. Lehmann, S.P. Sane, Wing rotation and the aerodynamic basis of insect flight, Science 284 (1999) 1954-1960.

[2] J. Valasek, Morphing aerospace vehicles and structures, Wiley, Chichester, 2012.

[3] H. Wang, L.J. Zeng, H. Liu, C.Y. Yin, Measuring wing kinematics, flight trajectory and body attitude during forward flight and turning maneuvers in dragonflies, Journal of Experimental Biology 206 (2003) 745-757.

[4] W. Shyy, Y. Liang, J. Tang, D. Viieru, H. Liu, Aerodynamics of Low Reynolds Number Flyers.

[5] T. Lee, Y.Y. Su, Lift enhancement and flow structure of airfoil with joint trailing-edge flap and Gurney flap, Experiments in Fluids 50 (2011) 1671-1684.

[6] C.M. Ho, Y.C. Tai, Review: MEMS and its applications for flow control, Journal of Fluids Engineering-Transactions of the Asme 118 (1996) 437-447.

[7] T.A.W. Brian C. Prock, and William A. Crossley, Morphing Airfoil Shape Change Optimization with Minimum Actuator Energy as an Objective, 9th AIAA/ISSMO Symposium on Multidisciplinary Analysis and Optimization, Atlanta, Georgia, 2002.

[8] Z.J. Wang, J.M. Birch, M.H. Dickinson, Unsteady forces and flows in low Reynolds number hovering flight: two-dimensional computations vs robotic wing experiments, Journal of Experimental Biology 207 (2004) 449-460.

[9] J.D. Eldredge, Numerical simulation of the fluid dynamics of 2D rigid body motion with the vortex particle method, Journal of Computational Physics 221 (2007) 626-648.

[10] F.a.J. Manar, Anya R., The Eect of Tip Clearance on Low Reynolds Number Rotating Wings, AIAA Aerospace Sciences Meeting, National Harbor, Maryland, January, 2014.

[11] Z.J. Wang, DISSECTING INSECT FLIGHT, 2005, pp. 183-210.

[12] P. Freymuth, Thrust Generation by an Airfoil in Hover Modes, Experiments in Fluids 9 (1990) 17-24.

[13] P. Trizila, C.K. Kang, H. Aono, W. Shyy, M. Visbal, Low-Reynolds-Number Aerodynamics of a Flapping Rigid Flat Plate, AIAA Journal 49 (2011) 806-823.

[14] L. Zheng, T. Hedrick, R. Mittal, A comparative study of the hovering efficiency of flapping and revolving wings, Bioinspiration & Biomimetics 8 (2013).

[15] M.S. Triantafyllou, G.S. Triantafyllou, An efficient swimming machine, Scientific american 272 (1995) 64-71.

[16] J.M. Anderson, K. Streitlien, D.S. Barrett, M.S. Triantafyllou, Oscillating foils of high propulsive efficiency, Journal of Fluid Mechanics 360 (1998) 41-72.

[17] F. Noca, D. Shiels, D. Jeon, MEASURING INSTANTANEOUS FLUID DYNAMIC FORCES ON BODIES, USING ONLY VELOCITY FIELDS AND THEIR DERIVATIVES, Journal of Fluids and Structures 11 (1997) 345-350.

[18] J.Z. Wu, H.Y. Ma, M.D. Zhou, Vorticity and Vortex Dynamics, Springer, 2006.

[19] M.F. Platzer, K.D. Jones, J. Young, J.C.S. Lai, Flapping-wing aerodynamics: Progress and challenges, AIAA Journal 46 (2008) 2136-2149.

[20] Cazemier, Proper orthogonal decomposition and low-dimensional models for driven cavity flows, Physics of Fluids 10 (1998) 1685.

[21] K.E. Meyer, J.M. Pedersen, O. Özcan, A turbulent jet in crossflow analysed with proper orthogonal decomposition, Journal of Fluid Mechanics 583 (2007) 199-227.

[22] R. Perrin, M. Braza, E. Cid, S. Cazin, A. Barthet, A. Sevrain, C. Mockett, F. Thiele, Obtaining phase averaged turbulence properties in the near wake of a circular cylinder at high Reynolds number using POD, Experiments in Fluids 43 (2007) 341-355.

[23] L.-H. Feng, J.-J. Wang, C. Pan, Proper orthogonal decomposition analysis of vortex dynamics of a circular cylinder under synthetic jet control, Physics of Fluids 23 (2011) 014106-014113.

[24] E. Konstantinidis, S. Balabani, M. Yianneskis, Bimodal vortex shedding in a perturbed cylinder wake, Physics of Fluids 19 (2007) 011701.

[25] J. Paik, C. Escauriaza, F. Sotiropoulos, On the bimodal dynamics of the turbulent horseshoe vortex system in a wing-body junction, Physics of Fluids 19 (2007).

[26] V. Kitsios, L. Cordier, J.P. Bonnet, A. Ooi, J. Soria, On the coherent structures and stability properties of a leading-edge separated aerofoil with turbulent recirculation, Journal of Fluid Mechanics 683 (2011) 395-416.

[27] H. Dong, R. Mittal, F.M. Najjar, Wake topology and hydrodynamic performance of low-aspect-ratio flapping foils, Journal of Fluid Mechanics 566 (2006) 309-343.

[28] H.M. Blackburn, F. Marques, J.M. Lopez, Symmetry breaking of two-dimensional time-periodic wakes, Journal of Fluid Mechanics 522 (2005) 395-411.

[29] J.C.R. Hunt, A.A. Wray, P. Moin, Eddies, streams, and convergence zones in turbulent flows, Center for Turbulence Research Report CTR-S88 (1988).

[30] C.W. Rowley, Model reduction for fluids, using balanced proper orthogonal decomposition, International Journal of Bifurcation and Chaos 15 (2005) 997-1013.

[31] P.J. Schmid, Dynamic mode decomposition of numerical and experimental data, Journal of Fluid Mechanics 656 (2010) 5-28.

[32] Yun Liu, Bo Cheng, Xinyan Deng, " An application of smoke-wire visualization on a hovering insect wing", Journal of Visualization Vol:**16** , 2013

[33] Yun Liu, Bo Cheng,Giovanni Barbera, Daniel R Troolin, Xinyan Deng, "Volumetric Visualization of the near- and far- field wake in flapping wings" Bioinspiration & Biommetics Vol: 8 No.3, 2013

[34] Yun Liu, Bo Cheng, Xinyan Deng, "An Experimental Study of Dynamic Trailing Edge Defections on a Two Dimensional Translating Wing" AIAA paper 2013-2816

[35] B Cheng, SP Sane, G Barbera, DR Troolin, T Strand, X Deng " Three-dimensional flow visualization and vorticity dynamics in revolving wings" Exp in fluids 54(1),2013

[36] B. Cheng, J. Roll, Y. Liu, D. R. Troolin, and X. Deng. "Three dimensional Vortex Wake Structure of Flapping Wings in Hovering Flight", Journal of Royal Society Interface, Vol **11,** 2014

[37] Yun Liu, Bo Cheng, Sanjay P Sane, Xinyan Deng, "Aerodynamics of dynamic wing deflection in translating wings" Under review in Exp. in fluids. 2014

[38] Liang Zhao, Xinyan Deng, "Aerodynamics effects of cambered wing " submitted

5. Performance Metric

5.1 Peer-reviewed Journal and Conference Papers

1. Z. Gaston, H. Wan, H. Dong, and M. Ol, "Analysis of Hinge-Connected Flapping Plate with an Implemented Torsional Spring Model", 50th AIAA Aerospace Sciences Meeting, AIAA 2012-0298, Nashville, Tennessee, Jan. 09-12, 2012

2. Z. Liang, H. Wan, H. Dong, and P. Beran, "Unsteady Flow and Its Reduced Order Modeling of Finite-Aspect-Ratio Foils", 50th AIAA Aerospace Sciences Meeting, AIAA 2012-1207, Nashville, Tennessee, Jan. 09-12, 2012

3. H. Wan, H. Dong, and Z. Liang, "Vortex Formation of Freely Falling Plates", 50th AIAA Aerospace Sciences Meeting, AIAA 2012-1207, Nashville, Tennessee, Jan. 09-12, 2012

4. H. Wan, H. Dong, and G. P. Huang, "Hovering Hinge Connected Flapping Plate with Passive Deflection", AIAA Journal, Vol. 5, No.9, 2012

5. H. Wan, H. Dong, C. Li, and Z. Liang, "Vortex Formation and Aerodynamic Force of Low Aspect-Ratio Plate in Translation and Rotation", 42nd AIAA Fluid Dynamics Conference and Exhibit, AIAA 2012-3278, New Orleans, Louisiana, Jun. 25-28, 2012

6. C. Li, and H. Dong, "Computational Investigation of Flow Structure and Aerodynamic Performance in Low Aspect Ratio Revolving Plates at Low Reynolds number", 52nd Aerospace Sciences Meeting, AIAA 2014-1453, National Harbor, Maryland, Jan. 13-17, 2014

7. C. Li, H. Dong, and Y. Ren, "A Numerical Study of Flapping Plates Hinged with a Trailing-Edge Flap", 32nd Aerospace Sciences Meeting, AIAA paper (to appear), Atlanta, Georgia, Jun. 16-20, 2014

8. Z. Liang, "Computational Analysis of Vortex Structures in Flapping Flight", PhD dissertation, Mechanical and Materials Engineering, Wright State University, 2013

9. C. Li, "Unsteady Flow and Aerodynamic Effect of a Dynamic Trailing-Edge Flap in Flapping Flight", Master thesis, Mechanical and Aerospace Engineering, University of Virginia, 2014

10. Yun Liu, Bo Cheng, Xinyan Deng, " An application of smoke-wire visualization on a hovering insect wing", Journal of Visualization Vol:**16** , 2013

11. Yun Liu, Bo Cheng,Giovanni Barbera, Daniel R Troolin, Xinyan Deng, "Volumetric Visualization of the near- and far- field wake in flapping wings" Bioinspiration & Biommetics Vol: 8 No.3, 2013
12. Yun Liu, Bo Cheng, Xinyan Deng, "An Experimental Study of Dynamic Trailing Edge Defections on a Two Dimensional Translating Wing" AIAA paper 2013-2816
13. B Cheng, SP Sane, G Barbera, DR Troolin, T Strand, X Deng " Three-dimensional flow visualization and vorticity dynamics in revolving wings" Exp in fluids 54(1),2013
14. B. Cheng, J. Roll, Y. Liu, D. R. Troolin, and X. Deng. "Three dimensional Vortex Wake Structure of Flapping Wings in Hovering Flight", Journal of Royal Society Interface, Vol **11,** 2014
15. Yun Liu, Bo Cheng, Sanjay P Sane, Xinyan Deng, "Aerodynamics of dynamic wing deflection in translating wings" Under review in Exp. in fluids. 2014

5.2 Awards and media exposure

1. Haibo Dong, Award for outstanding contribution to the Mechanical Engineering students of UVa. May 2014.
2. *The UVa Magazine,* July 2013 "Flight of the Cicadas".
3. *UVa Today,* July 30, 2013 "Engineering Team Studying Insect Flight to Build Robots".
4. *2013 UVA president's Report,* Discovering the Joys of Research.
5. *The American Scholar* Vol 83, No. 2, Spring 2014 "Secrets of Dragonflies".

5.3 Students support

Hui Wan (Postdoc), Geng Liu (Postdoc), Zongxian Liang (PhD student), Yan Ren, Chengyu Li (Master Student), Zach Gaston (Master Student)

Bo Cheng (Postdoc), Yun Liu (PhD student)